

# A matrix-free convex limiting framework for continuous Galerkin methods with nonlinear stabilization

Dmitri Kuzmin\*, Hennes Hajduk, Joshua Vedral

*Institute of Applied Mathematics (LS III), TU Dortmund University  
Vogelpothsweg 87, D-44227 Dortmund, Germany*

---

## Abstract

We equip a high-order continuous Galerkin discretization of a general hyperbolic problem with a nonlinear stabilization term and introduce a new methodology for enforcing preservation of invariant domains. The amount of shock-capturing artificial viscosity is determined by a smoothness sensor that measures deviations from a weighted essentially nonoscillatory (WENO) reconstruction. Since this kind of dissipative stabilization does not guarantee that the nodal states of the finite element approximation stay in a convex admissible set, we adaptively constrain deviations of these states from intermediate cell averages. The representation of our scheme in terms of such cell averages makes it possible to apply convex limiting techniques originally designed for positivity-preserving discontinuous Galerkin (DG) methods. Adapting these techniques to the continuous Galerkin setting and using Bernstein polynomials as local basis functions, we prove the invariant domain preservation property under a time step restriction that can be significantly weakened by using a flux limiter for the auxiliary cell averages. The close relationship to DG-WENO schemes is exploited and discussed. All algorithmic steps can be implemented in a matrix-free and hardware-aware manner. The effectiveness of the new element-based limiting strategy is illustrated by numerical examples.

*Keywords:* hyperbolic problems, invariant domain preservation, high-order finite elements, WENO stabilization, monolithic convex limiting

---

\*Corresponding author

*Email addresses:* [kuzmin@math.uni-dortmund.de](mailto:kuzmin@math.uni-dortmund.de) (Dmitri Kuzmin),  
[hennes.hajduk@math.tu-dortmund.de](mailto:hennes.hajduk@math.tu-dortmund.de) (Hennes Hajduk),  
[joshua.vedral@math.tu-dortmund.de](mailto:joshua.vedral@math.tu-dortmund.de) (Joshua Vedral)

---

## 1. Introduction

Finite element methods based on continuous Galerkin (CG) approximations are rarely used for discretization of nonlinear hyperbolic problems. It is commonly believed that finite volume and discontinuous Galerkin (DG) methods are better suited for this purpose because of the ease with which they can be manipulated to satisfy physical and numerical admissibility conditions. In particular, the use of slope limiters makes it possible to enforce preservation of local and/or global bounds for scalar quantities of interest [5, 24, 64]. Since slope limiting does not preserve global continuity, high-resolution finite element schemes of CG type are usually stabilized using nonlinear artificial viscosity [9, 10, 19, 21] or algebraic flux correction (AFC) tools [27, 30].

Many classical AFC schemes for low-order (linear or multilinear) continuous finite elements belong to the family of flux-corrected transport (FCT) methods [31, 41]. In the scalar case, flux limiting can be performed using Zalesak’s algorithm [62] or a localized limiter for individual edge or element contributions [7, 12, 40]. Both approaches can be generalized to systems in a manner that guarantees the validity of positivity constraints for quasi-concave scalar functions of conserved variables [8, 9, 39]. Numerical schemes that provably satisfy such inequality constraints are called invariant domain preserving (IDP) [11] or, informally, positivity preserving [64].

The localized FCT method proposed by Guermond et al. [9] constrains forward Euler stages of an explicit strong stability preserving Runge–Kutta (SSP-RK) method using *convex limiting*. This terminology reflects the fact that the nodal states of the flux-corrected CG approximation represent convex combinations of admissible states. The IDP property of the low-order (local Lax–Friedrichs) method, and of the FCT extension, is guaranteed under a CFL-like time step restriction. The *monolithic* convex limiting (MCL) procedure introduced in [25] can be combined with any time stepping method [35, 45, 50] and has been successfully extended to high-order finite elements [33, 34]. Convex limiting of FCT or MCL type is also possible for nodal DG methods using Bernstein or Legendre–Gauss–Lobatto (LGL) finite elements of arbitrary order [14, 15, 38, 47, 51]. However, achieving optimal accuracy and performance with such AFC schemes typically requires the use of compact-stencil representations, subcell flux limiters, and local bounds depending on *ad hoc* smoothness indicators (as shown already in [16, 17, 34, 40]).

A powerful alternative framework for the design of positivity-preserving high-order DG methods was developed by Zhang and Shu [63, 64, 65]. In a typical implementation of their approach, which builds on the seminal paper [48] by Perthame and Shu, spurious oscillations are suppressed by using a weighted essentially nonoscillatory (WENO) reconstruction as a substitute for an unacceptable DG approximation in a troubled cell [43, 49, 52, 66, 67, 68, 69]. Positivity preservation can then be enforced using slope or flux limiting. The Zhang–Shu slope limiter ensures positivity at the quadrature points corresponding to a convex decomposition of the cell average into states that are evolved using a one-dimensional IDP scheme [27, 64]. Flux limiting makes it possible to constrain the cell averages directly [44, 60, 61]. In particular, FCT and MCL algorithms can be used for this purpose [13, 26, 27].

The objective of this work is to develop a CG version of the Zhang–Shu limiting machinery for DG discretizations of hyperbolic problems. The first step toward that end has already been made in [36], where we designed nonlinear stabilization terms for CG discretizations using shock detectors that depend on deviations from a Hermite WENO reconstruction. In contrast to traditional WENO limiters, our approach is suitable for baseline discretizations of CG type and leads to analyzable nonlinear schemes [56]. It remains to design a limiter that ensures positivity preservation. The convex limiting strategy that we propose below is based on a representation of the CG approximation in terms of constrained nodal states. An element-based slope limiter controls deviations of these states from intermediate cell averages that are positivity preserving under a restrictive CFL condition. The optional use of a flux limiter enables us to guarantee positivity preservation under the mild CFL condition of the piecewise-constant DG- $\mathbb{P}_0$  approximation. Moreover, all calculations can be performed in a matrix-free manner, i.e., without calculating the full element matrices of the high-order finite element space. This desirable property of stabilized schemes paves the way for achieving high performance in hardware-oriented implementations [4, 6, 16, 17, 22].

In Section 2, we discretize a generic hyperbolic problem in space using Bernstein finite elements and the CG-WENO method introduced in [36]. As we show in Section 3, the stabilized baseline scheme can be decomposed into a low-order IDP approximation and a sum of element contributions that may require limiting. Representing the low-order part in terms of intermediate cell averages, we formulate sufficient conditions for explicit SSP-RK time discretizations to be IDP. Monolithic limiters for auxiliary cell averages and auxiliary nodal states are presented in Section 4. Finally, we perform

numerical studies and draw conclusions in Sections 5 and 6, respectively.

## 2. Stabilized CG discretization

Let  $u(\mathbf{x}, t)$  denote a conserved quantity or a vector of conserved variables depending on the space location  $\mathbf{x}$  and time instant  $t \geq 0$ . Restricting our attention to a bounded domain  $\Omega \subset \mathbb{R}^d$ ,  $d \in \{1, 2, 3\}$  and choosing a flux function  $\mathbf{f}(u)$ , we consider the (possibly nonlinear) hyperbolic problem

$$\frac{\partial u}{\partial t} + \nabla \cdot \mathbf{f}(u) = 0 \quad \text{in } \Omega \times (0, T], \quad (1a)$$

$$u(\cdot, 0) = u_0 \quad \text{in } \Omega, \quad (1b)$$

$$\mathbf{f}(u) \cdot \mathbf{n} = \mathcal{F}(u, \hat{u}; \mathbf{n}) \quad \text{on } \partial\Omega \times [0, T], \quad (1c)$$

where  $u_0$  is the initial data,  $T > 0$  is the final time, and  $\hat{u}$  is the data of a weakly imposed boundary condition. We denote by  $\mathcal{F}(u_L, u_R; \mathbf{n})$  a boundary flux in the direction of the unit outward normal  $\mathbf{n}$ . The states  $u_L$  and  $u_R$  represent the initial states of the corresponding Riemann problem [27].

An invariant domain of problem (1) is a convex admissible set  $\mathcal{G}$  such that  $u(\mathbf{x}, t) \in \mathcal{G}$  for all space-time locations  $(\mathbf{x}, t)$ . In particular, this definition implies that  $u_0(\mathbf{x}) \in \mathcal{G}$  for all  $\mathbf{x} \in \Omega$  and  $\hat{u}(\mathbf{x}, t) \in \mathcal{G}$  for all  $(\mathbf{x}, t) \in \partial\Omega \times [0, T]$ .

### 2.1. Galerkin scheme using Bernstein finite elements

To solve (1) using a CG-type finite element method, we use a conforming, possibly unstructured, mesh  $\mathcal{T}_h$  consisting of simplices or  $d$ -dimensional boxes  $K_e$ ,  $e = 1, \dots, E_h$ . For simplicity, we assume that  $\bar{\Omega} = \bigcup_{e=1}^{E_h} K_e$ . A globally continuous approximation  $u_h$  is sought in a space  $V_h$  that is spanned by nodal basis functions  $\varphi_1, \dots, \varphi_{N_h} \in C(\bar{\Omega})$  of polynomial degree  $p \in \mathbb{N}$ . The corresponding nodal points are denoted by  $\mathbf{x}_1, \dots, \mathbf{x}_{N_h}$ . The basis functions  $\varphi_i$  of the Bernstein polynomial basis are nonnegative and form a partition of unity, i.e.,  $\sum_{i=1}^{N_h} \varphi_i \equiv 1$ . For a formal definition of  $\varphi_i$  and a review of further properties, we refer the reader to [14, 33, 34, 40] and [27, Sec. 6.1].

Adopting the Bernstein basis representation, we store the global indices of nodes belonging to a macrocell  $K_e$  in the integer set  $\mathcal{N}_e$  such that

$$u_h|_{K_e} = \sum_{j \in \mathcal{N}_e} u_j \varphi_j, \quad e = 1, \dots, E_h.$$

The indices of macrocells containing a nodal point  $\mathbf{x}_i$  are stored in the integer set  $\mathcal{E}_i$ . The boundary  $\partial K_e$  of  $K_e$  consists of facets  $S_{ee'}$ . We define  $\mathcal{B}_e$  as

the set of cell indices such that  $S_{ee'} = \partial K_e \cap \partial K_{e'}$  for  $e' \in \{1, \dots, E_h\} \setminus \{e\}$ . A unique index  $e' > E_h$  is associated with each boundary facet  $S_{ee'} \subset \partial\Omega$ . The set  $\mathcal{B}_e^\partial = \{e' \in \mathcal{B}_e : e' > E_h\}$  contains the indices of such facets.

The standard CG approximation  $u_h \in V_h$  to a weak solution of (1) satisfies

$$\begin{aligned} \sum_{e=1}^{E_h} \int_{K_e} v_h \left[ \frac{\partial u_h}{\partial t} + \nabla \cdot \mathbf{f}(u_h) \right] d\mathbf{x} \\ + \sum_{e=1}^{E_h} \int_{\partial K_e \cap \partial\Omega} v_h [\mathcal{F}(u_h, \hat{u}_h; \mathbf{n}) - \mathbf{f}(u_h) \cdot \mathbf{n}] ds = 0 \end{aligned}$$

for any test function  $v_h \in V_h$ . Introducing the notation

$$(v_h, u_h) = \sum_{e=1}^{E_h} \int_{K_e} v_h u_h d\mathbf{x}, \quad (2)$$

$$a(v_h, u_h) = \sum_{e=1}^{E_h} \int_{K_e} v_h \nabla \cdot \mathbf{f}(u_h) d\mathbf{x}, \quad (3)$$

$$b(v_h, u_h, \hat{u}_h) = \sum_{e=1}^{E_h} \int_{\partial K_e \cap \partial\Omega} v_h [\mathcal{F}(u_h, \hat{u}_h; \mathbf{n}) - \mathbf{f}(u_h) \cdot \mathbf{n}] ds, \quad (4)$$

we write the semi-discrete problem in the form

$$\frac{d}{dt}(v_h, u_h) + a(v_h, u_h) + b(v_h, u_h, \hat{u}_h) = 0 \quad \forall v_h \in V_h. \quad (5)$$

The use of  $v_h \in \{\varphi_1, \dots, \varphi_{N_h}\}$  in (5) yields a system of semi-discrete nonlinear equations for the nodal states  $u_j(t)$  that define  $u_h = \sum_{j=1}^{N_h} u_j \varphi_j$ . Note that, in contrast to Lagrange finite elements, the identity  $u_j(t) = u_h(\mathbf{x}_j, t)$  generally holds only if the nodal point  $\mathbf{x}_j$  is a vertex of the mesh  $\mathcal{T}_h$ .

## 2.2. Dissipative WENO stabilization

To achieve optimal convergence and avoid spurious oscillations within the global bounds of IDP constraints, we add a nonlinear stabilization term

$$s_h(v_h, u_h) = \sum_{e=1}^{E_h} s_h^e(v_h, u_h)$$

on the left-hand side of (5). The CG-WENO methods presented in [36, 56] blend the local bilinear forms of high- and low-order stabilization operators

using a smoothness sensor  $\gamma_e \in [0, 1]$ . The element contributions

$$s_h^e(v_h, u_h) = \nu_e \int_{K_e} \nabla v_h \cdot (\nabla u_h - \gamma_e \mathbf{g}_h) d\mathbf{x} \quad (6)$$

are defined using the consistent  $L^2$  projection  $\mathbf{g}_h$  of  $\nabla u_h$  into the CG space. The viscosity parameter  $\nu_e = \frac{\lambda_e h_e}{2p}$  depends on the local mesh size  $h_e$ , polynomial degree  $p$ , and a local bound  $\lambda_e$  for the maximum speed. Details regarding the calculation of  $\mathbf{g}_h$  and  $\lambda_e$  can be found in [33, 36, 40, 56].

In formula (6), the smoothness sensor  $\gamma_e$  acts as a slope limiter for the projected gradient  $\mathbf{g}_h$ . In the case  $\gamma_e = 0$ , the local bilinear form (6) introduces low-order stabilization of local Lax–Friedrichs type. The setting  $\gamma_e = 1$  corresponds to the linear high-order stabilization employed in [33, 40]. The symmetry and positive semi-definiteness of the corresponding bilinear form can be shown as in [46, Lem. 1]. The WENO shock detector

$$\gamma_e = 1 - \min \left( 1, \frac{\|u_h^e - u_h^{e,*}\|_e}{\|u_h^e\|_e} \right)^q \quad (7)$$

proposed in [36] measures deviations of  $u_h^e = u_h|_{K_e}$  from a WENO reconstruction  $u_h^{e,*}$ . The sensitivity of  $\gamma_e$  to these deviations can be varied by adjusting the parameter  $q \geq 1$ . The Sobolev semi-norm  $\|\cdot\|_e$  is defined by

$$\|v\|_e = \left( \sum_{1 \leq |\mathbf{k}| \leq p} h_e^{2|\mathbf{k}|-d} \int_{K_e} |D^{\mathbf{k}} v|^2 d\mathbf{x} \right)^{1/2} \quad \forall v \in H^p(K_e), \quad (8)$$

where  $\mathbf{k} = (k_1, \dots, k_d)$  is the multiindex of the partial derivative  $D^{\mathbf{k}} v$ .

Following the design of Hermite WENO limiters for DG methods [43, 67, 69], the reconstruction  $u_h^{e,*}$  is defined as a convex combination of candidate polynomials  $u_{h,l}^e$ ,  $l = 0, \dots, n_e$  with nonlinear weights [20]

$$\omega_l^e = \frac{\tilde{w}_l^e}{\sum_{k=0}^{n_e} \tilde{w}_k^e}, \quad \tilde{w}_l^e = \frac{w_l^{e,\text{lin}}}{\|u_{h,l}^e\|_e^r + \epsilon}$$

that depend on the choice of the linear weights  $w_l^{e,\text{lin}}$  and on the power  $r \in \mathbb{N}$ . The small parameter  $\epsilon > 0$  is used to avoid division by zero. The candidate polynomials  $u_{h,l}^e$  are constructed using Hermite interpolation from cells  $K_{e'}$  sharing a facet  $S_{ee'}$  with  $K_e$ . For details, we refer the reader to [36, 56].

The use of the test function  $v_h = \varphi_i$  in the stabilized WENO version

$$\frac{d}{dt}(v_h, u_h) + a(v_h, u_h) + b(v_h, u_h, \hat{u}_h) + s_h(v_h, u_h) = 0 \quad \forall v_h \in V_h \quad (9)$$

of the spatial semi-discretization (5) yields the evolution equation

$$(\varphi_i, \dot{u}_h) + a(\varphi_i, u_h) + b(\varphi_i, u_h, \hat{u}_h) + s_h(\varphi_i, u_h) = 0, \quad (10)$$

where  $\dot{u}_h = \sum_{j=1}^{N_h} \dot{u}_j \varphi_j$  denotes the time derivative of  $u_h$ . Discretization in time can be performed, e.g., using an explicit SSP-RK method.

### 3. Low-order IDP discretization

In many cases, the results produced by the fully discrete version of the CG-WENO scheme (9) are excellent [36, 56]. However, there is no guarantee that the nodal states  $u_j$  of the Bernstein finite element approximation are positivity preserving / IDP. To show that the IDP property can be enforced using monolithic convex limiting, we first approximate  $\mathbf{f}(u_h)$  by

$$\mathbf{f}_h = \sum_{j=1}^{N_h} \mathbf{f}(u_j) \varphi_j \quad (11)$$

and define the low-order counterpart

$$m_i \frac{du_i}{dt} + a_i(u_h) + s_i(u_h) + b_i(u_h, \hat{u}_h) = 0 \quad (12)$$

of the semi-discrete equation (10) using (cf. [27, Ch. 3 and 6], [29])

$$m_i = \sum_{e \in \mathcal{E}_i} m_i^e, \quad m_i^e = \int_{K_e} \varphi_i d\mathbf{x}, \quad (13)$$

$$a_i(u_h) = \sum_{e \in \mathcal{E}_i} \frac{m_i^e}{|K_e|} \int_{K_e} \nabla \cdot \mathbf{f}_h d\mathbf{x} = \sum_{e \in \mathcal{E}_i} \frac{m_i^e}{|K_e|} \sum_{e' \in \mathcal{B}_e} \int_{S_{ee'}} \mathbf{f}_h \cdot \mathbf{n} ds, \quad (14)$$

$$s_i(u_h) = \sum_{e \in \mathcal{E}_i} s_i^e(u_h), \quad s_i^e(u_h) = \frac{m_i^e}{\Delta t_e} (u_i - u^e), \quad (15)$$

$$b_i(u_h, \hat{u}_h) = \sum_{e \in \mathcal{E}_i} \sum_{e' \in \mathcal{B}_e^0} \sigma_{i,ee'} [\mathcal{F}(u_i, \hat{u}_{i,ee'}; \mathbf{n}) - \mathbf{f}(u_i)], \quad (16)$$

$$\sigma_{i,ee'} = \int_{S_{ee'}} \varphi_i ds, \quad \hat{u}_{i,ee'} = \frac{1}{\sigma_{i,ee'}} \int_{S_{ee'}} \varphi_i \hat{u}_h ds. \quad (17)$$

The stabilization term  $s_i(u_h)$  introduces low-order *Rusanov dissipation* (cf. [1], [27, Ch. 4]), the levels of which are inversely proportional to a ‘fake’ time step  $\Delta t_e$ . An IDP upper bound for  $\Delta t_e$  is derived below. The nonlinear term  $a_i(u_h)$  of the evolution equation (12) approximates  $a(\varphi_i, u_h)$  using (11) and inexact quadrature for the integral  $\int_{K_e} \varphi_i \nabla \cdot \mathbf{f}_h d\mathbf{x}$ . The approximation of  $(\varphi_i, u_h)$  by  $m_i u_i$  corresponds to mass lumping, which is equivalent to using inexact quadrature for  $L^2$  scalar products. For Bernstein finite elements  $m_i^e = \frac{|K_e|}{|\mathcal{N}_e|}$ , where  $|\mathcal{N}_e|$  is the cardinality of the index set  $\mathcal{N}_e$  and  $|K_e|$  is the  $d$ -dimensional volume of  $K_e$ . Similar mass lumping is performed in the boundary term (16), in which we use the local Lax–Friedrichs (LLF) flux

$$\mathcal{F}(u_L, u_R; \mathbf{n}) = \frac{\mathbf{f}(u_L) + \mathbf{f}(u_R)}{2} \cdot \mathbf{n} - \frac{\lambda_{LR}}{2}(u_R - u_L) \quad (18)$$

depending on the maximum speed  $\lambda_{LR}$  of the corresponding Riemann problem.

### 3.1. Intermediate cell averages

Let us first analyze the low-order scheme (12) under the simplifying assumption of periodic boundary conditions. Since  $b_i(u_h, \hat{u}_h) = 0$  in the periodic case, the ordinary differential equation (12) can be written as

$$m_i \frac{du_i}{dt} = \sum_{e \in \mathcal{E}_i} m_i^e \frac{\bar{u}^e - u_i}{\Delta t_e}, \quad (19)$$

where  $\Delta t_e$  is the fake time step of the Rusanov dissipation (15) and

$$\bar{u}^e = u^e - \frac{\Delta t_e}{|K_e|} \sum_{e' \in \mathcal{B}_e} \int_{S_{ee'}} \mathbf{f}_h \cdot \mathbf{n} ds \quad (20)$$

is an intermediate cell average depending on the old cell average

$$u^e = \frac{1}{|K_e|} \int_{K_e} u_h d\mathbf{x} = \frac{1}{|K_e|} \sum_{i \in \mathcal{N}_e} m_i^e u_i. \quad (21)$$

If (19) is discretized in time using an explicit SSP-RK method, then each intermediate stage is a forward Euler update of the form

$$m_i u_i^{\text{SSP}} = \sum_{e \in \mathcal{E}_i} m_i^e \left[ \left( 1 - \frac{\Delta t}{\Delta t_e} \right) u_i + \left( \frac{\Delta t}{\Delta t_e} \right) \bar{u}^e \right], \quad (22)$$



where  $\Delta t > 0$  is a global time step such that

$$\Delta t \leq \min_{1 \leq e \leq E_h} \Delta t_e. \quad (23)$$

Under this condition, (22) yields a convex combination  $u_i^{\text{SSP}}$  of the states  $u_i$  and  $\bar{u}^e$ ,  $e \in \mathcal{E}_i$ . If these states belong to a convex admissible set  $\mathcal{G}$ , then so does  $u_i^{\text{SSP}}$ . Hence, the choice of  $\Delta t_e$  should ideally guarantee that

$$u_j \in \mathcal{G} \quad \forall j \in \mathcal{N}_e \quad \Rightarrow \quad \bar{u}^e \in \mathcal{G}. \quad (24)$$

For an element  $K_e = [x_i, x_j]$ ,  $j = i + 1$  of a 1D mesh with local spacing  $h_e = |K_e|$ , the intermediate state  $\bar{u}^e$  defined by (20) reduces to

$$\bar{u}_{ij} = \frac{u_i + u_j}{2} - \frac{\Delta t_e}{h_e} [f(u_j) - f(u_i)]. \quad (25)$$

Representation of (semi-)discrete schemes in terms of such *bar states* provides a convenient framework for proving the IDP property of first-order schemes and convex limiting algorithms [9, 11, 18, 25, 27]. Suppose that

$$\lambda_{ij} \frac{\Delta t_e}{h_e} \leq \frac{1}{2}, \quad (26)$$

where  $\lambda_{ij}$  is a local bound for the maximum speed. Then the interpretation of  $\bar{u}_{ij}$  as a spatially averaged exact solution to the Riemann problem with initial states  $u_i$  and  $u_j$  proves that  $\bar{u}_{ij} \in \mathcal{G}$  whenever  $u_i, u_j \in \mathcal{G}$ .

In the multidimensional case, the bar states  $\bar{u}_{ij}$  and their flux-corrected counterparts are associated with pairs of neighbor nodes or cells. The representation of the SSP-RK stage (22) in terms of element-based intermediate states  $\bar{u}^e$  rather than their edge-based counterparts  $\bar{u}_{ij}$  opens a new avenue for analysis and design of multidimensional IDP schemes. Remarkably, formula (20) resembles an explicit update for a cell average of a DG approximation. Taking advantage of this fact, we will adapt the analysis of positivity-preserving DG schemes [63, 64, 65] to our continuous finite element approximations.

### 3.2. Conditional IDP properties

It turns out that the IDP condition (24) is, indeed, satisfied if  $\Delta t_e$  is sufficiently small. We state and prove this result in the following lemma.

**Lemma 1** *Let  $\bar{u}^e$  be the intermediate cell average defined by (20). Then the validity of (24) is guaranteed under a subcell CFL condition*

$$\Delta t_e \leq \Delta t_e^{\max} \quad (27)$$

with a computable upper bound  $\Delta t_e^{\max}$  that depends on the local maximum speed and the type of the finite element approximation on  $K_e$ .  $\square$

**Proof:** Adapting the proof technique employed in [27, Thm. 5.15], we will express  $\bar{u}^e$  as a convex combination of states that are evolved using the one-dimensional LLF scheme and, therefore, possess the IDP property.

Splitting the set  $\mathcal{N}_e$  into  $\mathcal{N}_e^\partial = \{i \in \mathcal{N}_e : \mathbf{x}_i \in \partial K_e\}$  and  $\mathcal{N}_e^0 = \mathcal{N}_e \setminus \mathcal{N}_e^\partial$ , we represent the old average  $u^e$  defined by (21) as follows:

$$u^e = \frac{1}{s} \left[ \frac{m_0^e}{|K_e|} u_0^e + \sum_{i \in \mathcal{N}_e^\partial} \frac{m_i^e}{|K_e|} u_i \right]. \quad (28)$$

In the case  $\mathcal{N}_e^0 \neq \emptyset$ , we use  $s = 1$ ,  $u_0^e = \frac{1}{m_0^e} \sum_{i \in \mathcal{N}_e^0} m_i^e u_i$  and  $m_0^e = \sum_{i \in \mathcal{N}_e^0} m_i^e$ . If  $K_e$  has no internal nodes, which is the case for  $\mathbb{P}_1/\mathbb{Q}_1$  and triangular  $\mathbb{P}_2$  elements, we use  $s = 2$ ,  $u_0^e = u^e$  and  $m_0^e = |K_e|$ , as in [27, Thm. 5.15].

Recalling the definition (11) of the flux approximation  $\mathbf{f}_h$ , we find that

$$\sum_{e \in \mathcal{B}_e} \int_{S_{ee'}} \mathbf{f}_h \cdot \mathbf{n} ds = \sum_{i \in \mathcal{N}_e^\partial} \mathbf{f}(u_i) \cdot \mathbf{c}_{i,e}, \quad \mathbf{c}_{i,e} = \int_{\partial K_e} \varphi_i \mathbf{n} ds.$$

The intermediate cell average (20) admits the convex decomposition

$$\bar{u}^e = \frac{1}{s} \left[ \frac{m_0^e}{|K_e|} \bar{u}_0^e + \sum_{i \in \mathcal{N}_e^\partial} \frac{m_i^e}{|K_e|} \bar{u}_i^e \right], \quad (29)$$

where

$$\bar{u}_i^e = u_i - \frac{s \Delta t_e}{m_i^e} |\mathbf{c}_{i,e}| (\mathcal{F}(u_i, u_i; \mathbf{n}_{i,e}) - \mathcal{F}(u_0^e, u_i; \mathbf{n}_{i,e})), \quad i \in \mathcal{N}_e^\partial, \quad (30)$$

$$\bar{u}_0^e = u_0^e - \frac{s \Delta t_e}{m_0^e} \sum_{i \in \mathcal{N}_e^\partial} |\mathbf{c}_{i,e}| (\mathcal{F}(u_0^e, u_i; \mathbf{n}_{i,e}) - \mathcal{F}(u_0^e, u_0^e; \mathbf{n}_{i,e})) \quad (31)$$

are intermediate states defined using the LLF flux (18) with the normal direction  $\mathbf{n}_{i,e} = \frac{\mathbf{c}_{i,e}}{|\mathbf{c}_{i,e}|}$ . Note that  $\mathcal{F}(u_i, u_i; \mathbf{n}) = \mathbf{f}(u_i) \cdot \mathbf{n}$  and

$$\begin{aligned}\mathcal{F}(u_i, u_i; \mathbf{n}_{i,e}) - \mathcal{F}(u_0^e, u_i; \mathbf{n}_{i,e}) &= \frac{\mathbf{f}(u_i) - \mathbf{f}(u_0^e)}{2} \cdot \mathbf{n}_{i,e} + \lambda_{0i}^e \frac{u_i - u_0^e}{2}, \\ \mathcal{F}(u_0^e, u_i; \mathbf{n}_{i,e}) - \mathcal{F}(u_0^e, u_0^e; \mathbf{n}_{i,e}) &= \frac{\mathbf{f}(u_i) - \mathbf{f}(u_0^e)}{2} \cdot \mathbf{n}_{i,e} - \lambda_{0i}^e \frac{u_i - u_0^e}{2}.\end{aligned}$$

Introducing the one-dimensional IDP bar states (cf. [11, 18])

$$\bar{u}_{0i}^e = \frac{u_i + u_0^e}{2} - \frac{\mathbf{f}(u_i) - \mathbf{f}(u_0^e)}{2\lambda_{0i}^e} \cdot \mathbf{n}_{i,e}$$

such that

$$\frac{\mathbf{f}(u_i) - \mathbf{f}(u_0^e)}{2} \cdot \mathbf{n}_{i,e} = \lambda_{0i}^e \left( \frac{u_i + u_0^e}{2} - \bar{u}_{0i}^e \right),$$

we express relations (30) and (31) as follows (cf. [11]):

$$\bar{u}_i^e = u_i + \frac{s\Delta t_e}{m_i^e} |\mathbf{c}_{i,e}| \lambda_{0i}^e (\bar{u}_{0i}^e - u_i), \quad i \in \mathcal{N}_e^\partial, \quad (32)$$

$$\bar{u}_0^e = u_0^e + \frac{s\Delta t_e}{m_0^e} \sum_{i \in \mathcal{N}_e^\partial} |\mathbf{c}_{i,e}| \lambda_{0i}^e (\bar{u}_{0i}^e - u_0^e). \quad (33)$$

If the fake time step  $\Delta t_e$  satisfies condition (27) with

$$\Delta t_e^{\max} = \frac{1}{s} \min \left\{ \min_{i \in \mathcal{N}_e^\partial} \frac{m_i^e}{|\mathbf{c}_{i,e}| \lambda_{0i}^e}, \frac{m_0^e}{\sum_{i \in \mathcal{N}_e^\partial} |\mathbf{c}_{i,e}| \lambda_{0i}^e} \right\}, \quad (34)$$

then  $\bar{u}_i^e$ ,  $i \in \mathcal{N}_e^\partial$  and  $\bar{u}_0^e$  are convex combinations of the IDP states that appear on the right-hand sides of (32) and (33), respectively. This proves the claimed IDP property of the convex combination (29).  $\square$

The proof of the lemma can be extended to the case of non-periodic boundary conditions. If the boundary term  $b_i(u_h, \hat{u}_h)$  defined by (16) is included on the right-hand side of (19), a generalization of (30) and (31) needs to be analyzed. Let  $\mathcal{B}_{i,e}$  be the subset of  $\mathcal{B}_e$  such that  $\varphi_i$  is not identically zero on  $S_{ee'}$  with  $e' \in \mathcal{B}_{i,e}$ . Introducing the additional notation

$$\mathbf{c}_{i,ee'} = \int_{S_{ee'}} \varphi_i \mathbf{n} ds, \quad \mathbf{n}_{i,ee'} = \frac{\mathbf{c}_{i,ee'}}{|\mathbf{c}_{i,ee'}|}, \quad u_{i,ee'} = \begin{cases} u_i & \text{if } e' \leq E_h, \\ \hat{u}_{i,ee'} & \text{if } e' > E_h \end{cases}$$

and assuming that  $\mathcal{N}_e^0 \neq \emptyset$  for simplicity, we arrive at (29) with  $s = 1$  and

$$\begin{aligned}\bar{u}_i^e &= u_i - \frac{\Delta t_e}{m_i^e} \sum_{e' \in \mathcal{B}_{i,e}} |\mathbf{c}_{i,ee'}| (\mathcal{F}(u_i, u_{i,ee'}; \mathbf{n}_{i,ee'}) - \mathcal{F}(u_0^e, u_i; \mathbf{n}_{i,ee'})), \quad i \in \mathcal{N}_e^\partial, \\ \bar{u}_0^e &= u_0^e - \frac{\Delta t_e}{m_0^e} \sum_{i \in \mathcal{N}_e^\partial} \sum_{e' \in \mathcal{B}_{i,e}} |\mathbf{c}_{i,ee'}| (\mathcal{F}(u_0^e, u_i; \mathbf{n}_{i,ee'}) - \mathcal{F}(u_0^e, u_0^e; \mathbf{n}_{i,ee'})).\end{aligned}$$

The CFL bounds for these LLF updates can again be derived as in [11, 27] using representations in terms of  $\bar{u}_{0i}^e$  and  $\bar{u}_{i,ee'}^e$ . The latter bar state is defined as in (25) but using the Riemann data  $\hat{u}_{i,ee'}$  in place of  $u_j$ . We leave the calculation of  $\Delta t_e^{\max}$  as an exercise to the reader. The flux-limited version of our method will be IDP under a simpler and weaker CFL condition.

An important practical implication of Lemma 1 is the following theorem.

**Theorem 1** *Suppose that the global time step  $\Delta t$  satisfies condition (23) and all local time steps  $\Delta t_e$  satisfy (27) with  $\Delta t_e^{\max}$  defined in the proof of Lemma 1. Then the fully discrete scheme (22) is IDP for  $i = 1, \dots, N_h$ .  $\square$*

**Proof:** The claim is true because (22) yields a convex combination  $u_i^{\text{SSP}}$  of the IDP states  $u_i$  and  $\bar{u}^e$ ,  $e \in \mathcal{E}_i$  under the assumptions of the theorem.  $\square$

In view of (15), the levels of Rusanov dissipation built into (12) are proportional to  $1/\Delta t_e$ . The naive choice  $\Delta t_e := \Delta t := \min_{1 \leq e' \leq E_h} \Delta t_{e'}^{\max}$  leads to an extremely diffusive approximation of global Lax–Friedrichs type. An appropriate choice of time steps satisfying (23) and (27) is given by

$$\Delta t_e = \Delta t_e^{\max}, \quad \Delta t = \min_{1 \leq e' \leq E_h} \Delta t_{e'}. \quad (35)$$

We call  $\Delta t_e$  a *fake* time step because, similarly to graph viscosity coefficients  $d_{ij}$  of edge-based LLF schemes [11, 31, 42], the value of  $\Delta t_e^{\max}$  is determined at the level of spatial semi-discretization (19) by the local maximum speed and the distance between the nodes of the Bernstein finite element.

As the degree  $p$  of the polynomial approximation is increased without changing the size of the macrocell  $K_e$ , the IDP bound of Lemma 1 becomes more restrictive. To make  $\Delta t_e^{\max}$  independent of  $p$ , we redefine  $\bar{u}^e$  as follows:

$$\bar{u}^e = u^e - \frac{\Delta t_e}{|K_e|} \sum_{e' \in \mathcal{B}_e} |S_{ee'}| \mathcal{F}(u^e, u^{e'}; \mathbf{n}_{ee'}). \quad (36)$$

That is, we approximate  $\mathbf{f}_h|_{S_{ee'}}$  by the LLF flux  $\mathcal{F}(u^e, u^{e'}; \mathbf{n}_{ee'})$ , where

$$\mathbf{n}_{ee'} = \frac{\mathbf{c}_{ee'}}{|\mathbf{c}_{ee'}|}, \quad \mathbf{c}_{ee'} = \sum_{i \in \mathcal{N}_e} \mathbf{c}_{i,ee'} = \int_{S_{ee'}} \mathbf{n} \, ds.$$

Importantly, the adjustment of numerical fluxes in the formula for  $\bar{u}^e$  does not affect the global conservation property of (19) and (22). At the same time, the assertions of Lemma 1 and Theorem 1 become valid for

$$\Delta t_e^{\max} = \frac{|K_e|}{\sum_{e' \in \mathcal{B}_e} |S_{ee'}| \lambda_{ee'}}. \quad (37)$$

The intermediate cell averages  $\bar{u}^e$  defined by (36) with  $\Delta t_e \leq \Delta t_e^{\max}$  are IDP for  $\Delta t_e^{\max}$  given by (37). We omit the formal proof because (36) has the same structure as the finite volume and DG schemes considered in [13, 26, 27]. Therefore, the IDP property of  $\bar{u}^e$  is guaranteed under the same macrocell CFL condition, which imposes the simple bound (37) on the time step.

**Remark 1** Instead of approximating (20) by (36), the time scale  $\Delta t_e$  of formula (20) can be initialized using (37). If this choice produces an unacceptable state  $\bar{u}^e \notin \mathcal{G}$ , the value of  $\Delta t_e$  should be decreased as much as necessary to obtain  $\bar{u}^e \in \mathcal{G}$ . We use this strategy in the 2D examples of Section 5. The IDP property is guaranteed for  $\Delta t_e$  satisfying (27) with  $\Delta t_e^{\max}$  defined in Lemma 1. Note that, in view of (23), the value of the global time step  $\Delta t$  is determined by the smallest local time step. Hence, there is no guarantee that  $\Delta t$  can be increased without changing the numerical fluxes as in (36).  $\square$

#### 4. Monolithic convex limiting

We are now ready to present a constrained high-order extension of the low-order IDP schemes analyzed in Section 3. Adopting the general design principles of monolithic convex limiting [25, 33, 34] and adapting them to our element-based setting, we consider semi-discrete schemes of the form

$$m_i \frac{du_i}{dt} = \sum_{e \in \mathcal{E}_i} m_i^e \frac{\bar{u}_i^e - u_i}{\Delta t_e}. \quad (38)$$

The low-order approximation (19) uses the intermediate states  $\bar{u}_i^e = \bar{u}^e$ . In the case of non-periodic boundary conditions, which we discussed in Section 3,

the average LLF flux across a boundary facet  $S_{ee'} \subset \partial\Omega$  is given by

$$f_{ee'}^\partial = \frac{1}{|S_{ee'}|} \sum_{j \in \mathcal{N}_e^\partial} |\mathbf{c}_{j,ee'}| \mathcal{F}(u_j, \hat{u}_{j,ee'}; \mathbf{n}_{j,ee'}), \quad e' \in \mathcal{B}_e^\partial.$$

Let us blend the averaged high-order flux

$$f_{ee'}^H = \begin{cases} \frac{1}{|S_{ee'}|} \int_{S_{ee'}} \mathbf{f}_h \cdot \mathbf{n} \, ds & \text{if } e' \leq E_h, \\ f_{ee'}^\partial & \text{if } e' > E_h \end{cases} \quad (39)$$

and its low-order counterpart

$$f_{ee'}^L = \begin{cases} \mathcal{F}(u^e, u^{e'}; \mathbf{n}_{ee'}) & \text{if } e' \leq E_h, \\ \mathcal{F}(u^e, \hat{u}^{e'}; \mathbf{n}_{ee'}) & \text{if } e' > E_h \end{cases} \quad (40)$$

using a correction factor  $\alpha_{ee'} = \alpha_{e'e}$  to be defined below. The resulting flux-limited version of formula (20) reads (cf. [26, 29])

$$\bar{u}^e = u^e - \frac{\Delta t_e}{|K_e|} \sum_{e' \in \mathcal{B}_e} |S_{ee'}| (\alpha_{ee'} f_{ee'}^H + (1 - \alpha_{ee'}) f_{ee'}^L). \quad (41)$$

If no facet of the cell  $K_e$  belongs to a non-periodic boundary, the choices  $\alpha_{ee'} = 1$  and  $\alpha_{ee'} = 0$  correspond to (20) and (36), respectively.

The high-order scheme (10) can also be written in the form (38) with  $\bar{u}_i^e = \bar{u}^e + f_i^e/m_i^e$ , where  $\bar{u}^e$  is defined by (41) with  $\alpha_{ee'} = 1 \, \forall e' \in \mathcal{B}_e$ . The *antidiffusive element contributions*  $f_i^e$  that recover (10) are given by

$$\begin{aligned} f_i^e = m_i^e(u_i - u^e) + \Delta t_e & \left[ \int_{K_e} \nabla \varphi_i \cdot (\mathbf{f}(u_h) - \mathbf{f}_h) \, d\mathbf{x} \right. \\ & - \int_{K_e} \left( \varphi_i - \frac{m_i^e}{|K_e|} \right) \nabla \cdot \mathbf{f}_h \, d\mathbf{x} - g_i^e \\ & \left. - s_h^e(\varphi_i, u_h) - \int_{K_e} \varphi_i (\dot{u}_h - \dot{u}_i) \, d\mathbf{x} \right], \end{aligned} \quad (42)$$

where

$$\begin{aligned} g_i^e = \frac{m_i^e}{|K_e|} & \left( \int_{\partial K_e \cap \partial\Omega} \mathbf{f}_h \cdot \mathbf{n} \, ds - \sum_{j \in \mathcal{N}_e^\partial} \sum_{e' \in \mathcal{B}_e^\partial} |\mathbf{c}_{j,ee'}| \mathcal{F}(u_j, \hat{u}_{j,ee'}; \mathbf{n}_{j,ee'}) \right) \\ & + \int_{\partial K_e \cap \partial\Omega} \varphi_i [\mathcal{F}(u_h, \hat{u}_h; \mathbf{n}) - \mathbf{f}_h \cdot \mathbf{n}] \, ds. \end{aligned} \quad (43)$$

The contribution of  $g_i^e$  vanishes in the periodic case and for indices  $i$  such that  $\mathbf{x}_i \notin \partial\Omega$ . If  $K_e$  has no nodes on  $\partial\Omega$ , then  $g_i^e = 0 \forall i \in \mathcal{N}_e$ , and the components of the element vector  $(f_i^e)_{i \in \mathcal{N}_e}$  satisfy the zero sum condition

$$\sum_{i \in \mathcal{N}_e} f_i^e = 0. \quad (44)$$

**Theorem 2** *The semi-discrete scheme (38) is equivalent to the CG-WENO scheme (10) for  $\bar{u}_i^e = \bar{u}^e + f_i^e/m_i^e$  with  $f_i^e$  defined by (42) and*

$$\bar{u}^e = u^e - \frac{\Delta t_e}{|K_e|} \sum_{e' \in \mathcal{B}_e} |S_{ee'}| f_{ee'}^H.$$

**Proof:** Recalling the definition (39) of the high-order flux  $f_{ee'}^H$  and using the assumptions of the theorem, we find that (38) can be written as

$$\begin{aligned} m_i \frac{du_i}{dt} &= \sum_{e \in \mathcal{E}_i} m_i^e \frac{\bar{u}_i^e - u_i}{\Delta t_e} = \sum_{e \in \mathcal{E}_i} \left( m_i^e \frac{\bar{u}^e - u_i}{\Delta t_e} + \frac{f_i^e}{\Delta t_e} \right) \\ &= \sum_{e \in \mathcal{E}_i} \left( m_i^e \frac{u^e - u_i}{\Delta t_e} - \frac{m_i^e}{|K_e|} \sum_{e' \in \mathcal{B}_e} |S_{ee'}| f_{ee'}^H + \frac{f_i^e}{\Delta t_e} \right) \\ &= \sum_{e \in \mathcal{E}_i} \left( m_i^e \frac{u^e - u_i}{\Delta t_e} - \frac{m_i^e}{|K_e|} \int_{K_e} \nabla \cdot \mathbf{f}_h d\mathbf{x} + \frac{f_i^e}{\Delta t_e} + g^e \right), \end{aligned}$$

where  $\int_{K_e} \nabla \cdot \mathbf{f}_h d\mathbf{x} = \int_{\partial K_e} \mathbf{f}_h \cdot \mathbf{n} ds$  and

$$\begin{aligned} g^e &= \frac{m_i^e}{|K_e|} \left( \int_{\partial K_e \cap \partial\Omega} \mathbf{f}_h \cdot \mathbf{n} ds - \sum_{j \in \mathcal{N}_e^\partial} \sum_{e' \in \mathcal{B}_e^\partial} |\mathbf{c}_{j,ee'}| \mathcal{F}(u_j, \hat{u}_{j,ee'}; \mathbf{n}_{j,ee'}) \right) \\ &= g_i^e - \int_{\partial K_e \cap \partial\Omega} \varphi_i [\mathcal{F}(u_h, \hat{u}_h; \mathbf{n}) - \mathbf{f}_h \cdot \mathbf{n}] ds. \end{aligned}$$

Using (42) and (43), we deduce that

$$\begin{aligned} m_i \frac{du_i}{dt} &= \sum_{e \in \mathcal{E}_i} \left[ \int_{K_e} \nabla \varphi_i \cdot (\mathbf{f}(u_h) - \mathbf{f}_h) d\mathbf{x} - \int_{K_e} \varphi_i \nabla \cdot \mathbf{f}_h d\mathbf{x} \right. \\ &\quad \left. - \int_{\partial K_e \cap \partial\Omega} \varphi_i [\mathcal{F}(u_h, \hat{u}_h; \mathbf{n}) - \mathbf{f}_h \cdot \mathbf{n}] ds \right. \\ &\quad \left. - s_h^e(\varphi_i, u_h) - \int_{K_e} \varphi_i (\dot{u}_h - \dot{u}_i) d\mathbf{x} \right] \end{aligned}$$

$$\begin{aligned}
&= - \sum_{e \in \mathcal{E}_i} \left[ \int_{K_e} \varphi_i \nabla \cdot \mathbf{f}(u_h) d\mathbf{x} \right. \\
&\quad + \int_{\partial K_e \cap \partial \Omega} \varphi_i [\mathcal{F}(u_h, \hat{u}_h; \mathbf{n}) - \mathbf{f}(u_h) \cdot \mathbf{n}] ds \\
&\quad \left. + s_h^e(\varphi_i, u_h) + \int_{K_e} \varphi_i (\dot{u}_h - \dot{u}_i) d\mathbf{x} \right] \\
&= -[a(\varphi_i, u_h) + b(\varphi_i, u_h, \hat{u}_h) + s_h(\varphi_i, u_h) + (\varphi_i, \dot{u}_h - \dot{u}_i)].
\end{aligned}$$

This proves that the scheme under investigation is equivalent to (10).  $\square$

In the process of convex limiting, we first ensure that (41) is IDP by choosing  $\Delta t_e$  small enough to satisfy the requirements of Lemma 1 or using  $\Delta t_e = \Delta t_e^{\max}$  defined by (37) and tuning the correction factors  $\alpha_{ee'} \in [0, 1]$ . Next, we calculate element-based correction factors  $\beta_e \in [0, 1]$  such that the IDP property of  $\bar{u}^e$  is preserved by the intermediate states

$$\bar{u}_i^e = \bar{u}^e + \beta_e f_i^e / m_i^e, \quad i \in \mathcal{N}_e. \quad (45)$$

The application of  $\beta_e$  to the element contributions  $f_i^e$ ,  $i \in \mathcal{N}_e$  can be interpreted as slope limiting of Barth–Jespersen type [5] in the scalar case and of Zhang–Shu type [63, 64, 65] in the case of a hyperbolic system.

The fully discrete version of the constrained scheme (38) is given by

$$m_i u_i^{\text{SSP}} = \sum_{e \in \mathcal{E}_i} m_i^e \left[ \left( 1 - \frac{\Delta t}{\Delta t_e} \right) u_i + \left( \frac{\Delta t}{\Delta t_e} \right) \bar{u}_i^e \right]. \quad (46)$$

Its IDP property is guaranteed under the global CFL condition (23) with fake time steps  $\Delta t_e = \Delta t_e^{\max}$  defined by (37) if the flux limiter is activated (otherwise at least for  $\Delta t_e$  satisfying condition (27) of Lemma 1).

It remains to choose the algorithms for calculating  $\alpha_{ee'}$  and  $\beta_e$ . The choices that we make in this work are based on our experience with convex limiting of FCT and MCL type (see [27, Ch. 4 and 6], [8, 14, 25, 26, 40]).

#### 4.1. Flux limiting

Since our formula (41) for the intermediate cell average  $\bar{u}^e$  has the structure of a fully discrete finite volume scheme, flux limiting can be performed using the localized FCT algorithms presented in [13, 26, 29]. In general, the correction factor  $\alpha_{ee'} \in [0, 1]$  must satisfy the symmetry condition

$$\alpha_{ee'} = \alpha_{e'e} \quad \forall e' \in \mathcal{B}_e \setminus \mathcal{B}_e^\partial \quad (47)$$



and ensure that  $\bar{u}^e \in \mathcal{G}$  for an invariant domain  $\mathcal{G}$  that is preserved by

$$\bar{u}^{e,L} = u^e - \frac{\Delta t_e}{|K_e|} \sum_{e' \in \mathcal{B}_e} |S_{ee'}| f_{ee'}^L \quad (48)$$

with the fake time step  $\Delta t_e = \Delta t_e^{\max}$ , where  $\Delta t_e^{\max}$  is given by (37).

The numerical fluxes that define the value of  $\bar{u}^e$  in (41) can be written as

$$f_{ee'} = \alpha_{ee'} f_{ee'}^H + (1 - \alpha_{ee'}) f_{ee'}^L = f_{ee'}^L - \bar{f}_{ee'}^A, \quad (49)$$

where  $\bar{f}_{ee'}^A = \alpha_{ee'} f_{ee'}^A$  is a limited counterpart of the antidiffusive flux

$$f_{ee'}^A = f_{ee'}^L - f_{ee'}^H.$$

For a general hyperbolic problem of the form (1), the representation of

$$\bar{u}^e = \bar{u}^{e,L} + \frac{\Delta t_e}{|K_e|} \sum_{e' \in \mathcal{B}_e} |S_{ee'}| \bar{f}_{ee'}^A = \sum_{e' \in \mathcal{B}_e} \frac{|S_{ee'}|}{|\partial K_e|} u_{ee'}$$

as a convex combination of the flux-corrected intermediate states

$$u_{ee'} = \bar{u}^{e,L} + \frac{|\partial K_e| \Delta t_e \bar{f}_{ee'}^A}{|K_e|} = \bar{u}^{e,L} + \alpha_{ee'} \frac{|\partial K_e| \Delta t_e f_{ee'}^A}{|K_e|}$$

reveals that  $\bar{u}^e \in \mathcal{G}$  if  $u_{ee'} \in \mathcal{G} \forall e' \in \mathcal{B}_e$ . The low-order approximation  $\bar{u}^{e,L}$  is IDP for our choice of  $\Delta t_e$ . If  $u_{ee'} \notin \mathcal{G}$  or  $u_{e'e} \notin \mathcal{G}$ , then the high-order target flux  $f_{ee'}^A = -f_{e'e}^A$  is unacceptable and requires limiting.

In the scalar case, local or global bounds  $u^{e,\min} \in \mathcal{G}$  and  $u^{e,\max} \in \mathcal{G}$  are imposed on the cell average  $\bar{u}^e$  defined by (41). The validity of the discrete maximum principle  $\bar{u}^e \in [u^{e,\min}, u^{e,\max}]$  is guaranteed for

$$\bar{f}_{ee'}^A = \begin{cases} \min\{f_{ee'}^A, f_{ee'}^{\max}\} & \text{if } f_{ee'}^A \geq 0, \\ \max\{f_{ee'}^A, f_{ee'}^{\min}\} & \text{if } f_{ee'}^A < 0, \end{cases} \quad (50)$$

where [26, 28, 29], [27, Sec. 5.3.1.1]

$$f_{ee'}^{\max} = \begin{cases} \min \left\{ \frac{|K_e|}{|\partial K_e|} \frac{u^{e,\max} - u^{e,L}}{\Delta t_e}, \frac{|K_{e'}|}{|\partial K_{e'}|} \frac{u^{e',L} - u^{e',\min}}{\Delta t_{e'}} \right\} & \text{if } e \leq E_h, \\ \frac{|K_e|}{|\partial K_e|} \frac{u^{e,\max} - u^{e,L}}{\Delta t_e} & \text{if } e > E_h, \end{cases}$$

$$f_{ee'}^{\min} = \begin{cases} \max \left\{ \frac{|K_e|}{|\partial K_e|} \frac{u^{e,\min} - u^{e,L}}{\Delta t_e}, \frac{|K_{e'}|}{|\partial K_{e'}|} \frac{u^{e',L} - u^{e',\max}}{\Delta t_{e'}} \right\} & \text{if } e \leq E_h, \\ \frac{|K_e|}{|\partial K_e|} \frac{u^{e,\min} - u^{e,L}}{\Delta t_e} & \text{if } e > E_h. \end{cases}$$

Note that the unnecessary and ill-conditioned calculation of a correction factor  $\alpha_{ee'} \in [0, 1]$  for  $\bar{f}_{ee'}^A = \alpha_{ee'} f_{ee'}^A$  is avoided in (50).

Guermond et al. [9, 13] present a general line search algorithm for finding  $\alpha_{ee'}$  that ensures positivity preservation for quasi-concave functions of the conserved variables. An explicit formula for such  $\alpha_{ee'}$  can be derived if the IDP constraints are linear or can be replaced with linear sufficient conditions, as shown in [25, 27, 45] for the Euler equations of gas dynamics. A very elegant pressure fix was derived by Abgrall et al. [3, 57] using the general framework of geometric quasi-linearization [59]. We use this approach to enforce positivity preservation for the pressure of the Euler system in Section 5.

**Remark 2** In contrast to the FCT-type convex limiting algorithms presented in [9, 13], we constrain the intermediate cell averages (41) of the semi-discrete scheme (38) instead of auxiliary states  $u_{ee'}^{\text{FCT}}$  that depend on the real (global) time step  $\Delta t$  rather than a fake (local) time step  $\Delta t_e$ . Therefore, our limiting strategy is monolithic in the sense that  $\alpha_{ee'}$  is independent of  $\Delta t$ .  $\square$

#### 4.2. Slope limiting

The intermediate nodal states  $\bar{u}_i^e$  of formula (45) can be constrained using one of the element-based convex limiting algorithms reviewed in [27, Ch. 4 and 6]. The localized FCT schemes developed in [7, 8, 40] define

$$\beta_e = \min_{i \in \mathcal{N}_e} \beta_{i,e} \quad (51)$$

using nodal correction factors  $\beta_{i,e} \in [0, 1]$  such that the IDP property of  $\bar{u}^e$  implies that of  $\bar{u}_i^e = \bar{u}^e + \beta_e f_i^e / m_i^e$  for any  $\beta_e \in [0, \beta_{i,e}]$ . Importantly, the multiplication by  $\beta_e$  preserves the zero-sum property (44) of the unlimited element contributions  $f_i^e$  in the absence of boundary terms.

To preserve global or local bounds  $u_i^{\min} \in \mathcal{G}$  and  $u_i^{\max} \in \mathcal{G}$  in the scalar case, we calculate  $\beta_{i,e}$  using the FCT formula [8, 16, 29, 40]

$$\beta_{i,e} = \begin{cases} \min \left\{ 1, \frac{m_i^e (u_i^{\max} - \bar{u}^e)}{f_i^e} \right\} & \text{if } f_i^e > 0, \\ \min \left\{ 1, \frac{m_i^e (u_i^{\min} - \bar{u}^e)}{f_i^e} \right\} & \text{if } f_i^e < 0, \\ 1 & \text{otherwise.} \end{cases} \quad (52)$$

As noticed in [40, Sec. 4.3], this definition of  $\beta_{i,e}$  has the same structure as the vertex-based version [24] of the Barth–Jespersen slope limiter [5].

In extensions to systems, the IDP property of  $\bar{u}_i^e$  can be enforced as in the work of Zhang and Shu [63, 64, 65] or using explicit formulas derived from linear sufficient conditions. Examples of element-based algorithms using closed-form IDP limiters for the compressible Euler equations can be found in [8] and [27, Ex. 4.16 and 5.14]. The positivity fix presented in [3, 57] can also be adapted to the element-based format. The framework of geometric quasi-linearization [59] can be used to derive  $\beta_{i,e}$  for general systems.

**Remark 3** The monolithic structure of the semi-discrete scheme (38) using the flux-corrected cell averages (41) is preserved by our slope limiting procedure. Similarly to the MCL schemes reviewed in [27], constraints are imposed at the level of spatial semi-discretization, which has a well-defined residual even in the steady state limit. This property distinguishes our approach from predictor-corrector FCT algorithms and classical slope limiters.  $\square$

#### 4.3. Matrix-free implementation

We have intentionally refrained from using matrix notation for our finite element schemes because all algorithmic steps can be performed without calculating global or local matrices. Even the system of equations (10) for the nodal time derivatives  $\dot{u}_j$  can be solved using a matrix-free iterative method [2]. The residuals of fully discrete schemes can be assembled from element vectors without generating full element matrices. By contrast, high-order extensions of the FCT and MCL schemes proposed in [9, 25, 31] require costly matrix computations or subcell decomposition procedures that involve solution of local problems with sparse graph Laplacians [14, 33, 34, 40].

### 5. Numerical results

Let us now apply the proposed methodology to hyperbolic test problems. If the exact entropy solution of the problem at hand is unknown, we compare our results with reference solutions obtained on very fine meshes using a finite volume scheme with LLF fluxes. In this numerical study, we use uniform structured meshes and initialize the Bernstein degrees of freedom by  $u_j(0) := u_0(\mathbf{x}_j)$  if the second-order accuracy of this approximation is sufficient for our purposes. Unless stated otherwise, we impose periodic boundary conditions and set the steepening parameter in (7) equal to  $q = 1$ . Discretization in time is performed using the third-order explicit SSP Runge–Kutta method with adaptive global time steps corresponding to  $\omega_{\text{CFL}} = 0.5$ ,

where  $\omega_{\text{CFL}} = \Delta t / \Delta t^{\text{max}}$  is a constant scaling factor for the sharp bound  $\Delta t^{\text{max}}$  of the CFL condition that guarantees the IDP property.

### 5.1. Scalar problems in 1D

In our numerical studies for scalar one-dimensional problems of the form (1), the invariant domain to be preserved is  $\mathcal{G} = [u^{\min}, u^{\max}]$  with  $u^{\min} = \min_{x \in \bar{\Omega}} u_0(x)$  and  $u^{\max} = \max_{x \in \bar{\Omega}} u_0(x)$ .

#### 5.1.1. Linear advection

The simplest useful test problem is the 1D linear transport equation corresponding to (1) with  $f(u) = u$  and  $\Omega = (0, 1)$ . That is, the initial data  $u_0$  is advected with constant velocity  $v = 1$ . The periodic boundary conditions  $u(0, t) = u(1, t)$  are imposed at the end points of  $\Omega$ . In this 1D example, the exact solution  $u(\cdot, t)$  coincides with  $u_0$  for all time instants  $t \in \mathbb{N}_0$ .

To begin, we advect the  $L^2(\Omega)$  projection  $u_h(\cdot, 0) \in V_h$  of the smooth initial profile  $u_0(x) = e^{-100(x-0.5)^2}$  to study the convergence behavior of the CG-WENO target scheme (10) and of its limited counterpart (38). The  $L^2(\Omega)$  errors at the final time  $t = 1$  and the corresponding estimated orders of convergence (EOC) for  $\mathbb{P}_1$  and  $\mathbb{P}_2$  elements are listed in Table 1.

$1/h$	$\mathbb{P}_1$				$\mathbb{P}_2$			
	WENO	EOC	WENO-L	EOC	WENO	EOC	WENO-L	EOC
32	8.84E-02		8.95E-02		6.51E-04		4.29E-03	
64	3.12E-02	1.50	3.13E-02	1.52	4.81E-05	3.76	8.24E-04	2.38
128	3.60E-03	3.11	3.61E-03	3.12	5.97E-06	3.01	1.59E-04	2.38
256	2.74E-04	3.72	2.76E-04	3.71	7.63E-07	2.97	3.04E-05	2.38
512	2.33E-05	3.55	2.85E-05	3.28	9.64E-08	2.98	5.89E-06	2.37

Table 1:  $L^2(\Omega)$  error norms and convergence rates for 1D advection of the smooth profile  $u_0(x) = e^{-100(x-0.5)^2}$  with velocity  $v = 1$  up to  $t = 1$ .

While the optimal convergence rate  $p + 1$  is attained or even exceeded by the target scheme for Bernstein finite elements of degree  $p \in \{1, 2\}$ , it turns out that even slope limiting w.r.t. global bounds is too restrictive in the  $\mathbb{P}_2$  case. The issue here is subtle and can be explained as follows: While the *pointwise values* of the exact solution remain within the range  $\mathcal{G} = [0, 1]$ , this is not necessarily the case for the *Bernstein coefficients*. This peculiarity of Bernstein-basis AFC schemes is the reason why constraining the degrees of freedom to stay in  $\mathcal{G}$  leads to peak clipping effects and a loss of accuracy in the neighborhood of smooth global extrema (cf. [17]). To achieve optimal convergence, we envision the use of collocated LGL spectral elements (cf. [47, 51]) in future implementations of the proposed methodology.

**Remark 4** We observed similar convergence behavior in numerical experiments for the nonlinear Burgers test from [36, Sec. 7.2]. The results (not shown here) confirm that the target scheme converges at the optimal rate  $p+1$ . The limited  $\mathbb{P}_1$  approximation ( $p = 1$ ) exhibits second-order convergence, but the imposition of global bounds on the Bernstein coefficients of the  $\mathbb{P}_2$  version prevented us from achieving full third-order accuracy.  $\square$

In the next linear advection test, we advect the initial profile [14]

$$u_0(x) = \begin{cases} 1 & \text{if } 0.2 \leq x \leq 0.4, \\ \exp(10) \exp(\frac{1}{0.5-x}) \exp(\frac{1}{x-0.9}) & \text{if } 0.5 < x < 0.9, \\ 0 & \text{otherwise,} \end{cases} \quad (53)$$

which is comprised of a discontinuous step function and a bump with  $C^\infty$ -regularity. The final time is again  $t = 1$ .

Using the fixed number  $N_h = 128$  of nodal points for Bernstein finite elements with polynomial degrees  $p \in \{1, 2, 4, 8, 16\}$ , we perform the linear advection test for the IDP methods presented in Sections 3 and 4. In algorithms that use the high-order cell average (20), the local bounds  $\Delta t_e$  of the CFL condition (23) may not exceed the threshold  $\Delta t_e^{\max}$  of Lemma 1. The use of the low-order cell average (36) ensures the IDP property for  $\Delta t_e^{\max}$  defined by the less restrictive CFL bound (37) of the finite volume LLF scheme. The flux-limited version (41) is IDP under the same CFL condition, which reduces to  $\frac{v\Delta t}{h} \leq \frac{1}{2}$  with  $v = 1$  for this particular test problem.

The results shown in Figs. 1a and 1b confirm that flux limiting can drastically mitigate the time step restrictions. Interestingly enough, the flux-corrected approximations even seem to be less diffusive than numerical solutions obtained without flux limiting but using smaller time steps. This behavior indicates that smearing effects tend to become less pronounced if fewer time steps are needed to reach the final time. It can also be observed that the low-order results become less accurate as the polynomial degree is increased while the mesh is coarsened to match the fixed value of  $N_h$ . In view of the findings reported in [16, 34, 40], this behavior is caused by the fact that the inherent Rusanov dissipation (15) lacks sparsity.

In our experience, the accuracy of the low-order solutions can be greatly improved by using the largest fake time step  $\Delta t_e$  that ensures the IDP property of  $\bar{u}^e$  for the given data. However, the results presented in Fig. 1a show that the accuracy of slope-limited high-order approximations is not

significantly affected by the levels of numerical dissipation in the low-order method corresponding to  $\beta_e = 0$ . As expected, the step function is slightly better captured with  $\mathbb{P}_1$  elements, while the  $\mathbb{P}_2$  version preserves the peak of the smooth bump with higher precision, despite the fact that the corresponding mesh is one level coarser than that for the  $\mathbb{P}_1$  simulation.

While it is remarkable that flux limiting ensures the validity of IDP constraints under the large-cell CFL condition, the requirement of stability for the unconstrained target (CG-WENO) scheme may dictate the use of smaller time steps in practice. If the target is unstable, violations of global bounds can be prevented by flux/slope limiters, but spurious oscillations may occur within these bounds, leading to unbounded growth of total variation or approximations of poor quality (see, e. g., [15, left panel of Fig. 3]). The CFL bound of the high-order scheme using Bernstein finite elements does depend on the polynomial degree and may be just marginally larger than the time step that meets the requirements of Lemma 1. Moreover, the efficiency gain resulting from the use of slightly larger  $\Delta t$  is diminished by the overhead cost associated with flux limiting. For spectral element approximations of LGL type, the CFL condition of the high-order discretization is far less severe than the IDP time step restriction (27) of Lemma 1. Hence, the possibility of optional flux limiting may lead to substantial speedups in the LGL version, which represents a promising alternative to Bernstein polynomials.

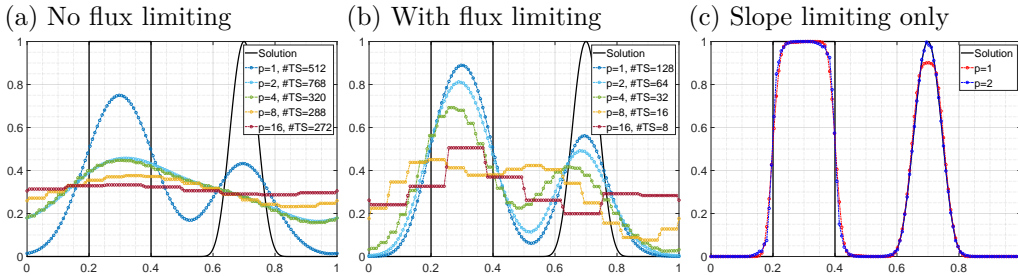


Figure 1: Low-order (a,b) and slope-limited (c) solutions to the 1D linear advection problem with initial condition (53) at  $t = 1$ . All approximations use  $N_h = 128$  nodes. The number of employed time steps is denoted by #TS.

### 5.1.2. Nonlinear problem with a nonconvex flux

Next, we consider the first of the two Riemann problems proposed in [23, Sec. 3.1] for the 1D nonlinear conservation law with the  $C^1(\mathbb{R})$  flux function

$$f(u) = \begin{cases} \frac{1}{4}u(1-u) & \text{if } u \leq \frac{1}{2}, \\ \frac{1}{2}u(u-1) + \frac{3}{16} & \text{otherwise.} \end{cases} \quad (54)$$

The domain  $\Omega = (0, 1)$  has an inlet at  $x = 0$  and an outlet at  $x = 1$ . The inflow boundary condition  $u(0, t) = 0$  is prescribed in this test. The initial condition is given by  $u_0(x) = \chi_{\{x \geq 1/4\}}$ , where  $\chi_X$  is the characteristic function of a set  $X \subset \Omega$ . The unique entropy solution consists of a shock propagating to the right and a rarefaction wave that connects the pre-shock value with the right state of the Riemann problem. A closed-form expression for the vanishing viscosity solution can be found in [27, Suppl. materials, Sec. A.4.2.2]. Many numerical methods fail to predict the pre-shock value correctly and yield profiles with piecewise-constant areas around the shock.

As in the previous example, we first use the low order methods to solve this problem up to the final time  $t = 1$  using a total of  $N_h = 129$  nodes for all combinations of polynomial degree  $p$  and mesh resolution  $h$ . The low-order results obtained without and with flux limiting are displayed in Figs. 2a and 2b. The slope-limited recovery of auxiliary nodal states  $\bar{u}_i^e$  from the unlimited high-order version of  $\bar{u}^e$  yields the approximations shown in Fig. 2c for  $p \in \{1, 2\}$ . Since the exact solution is piecewise linear in this test, the  $\mathbb{P}_1$  solution is more accurate than the  $\mathbb{P}_2$  approximation with the same number of nodes. However, the accuracy of the latter is still satisfactory.

Figure 2d shows the evolution of the total entropy  $\eta_\Omega(u) = \frac{1}{2} \int_\Omega u^2 dx$  for the slope-limited  $\mathbb{P}_1$  and  $\mathbb{P}_2$  approximations. We observe a monotone decrease of  $\eta_\Omega(u_h)$ , which is dominated by the outflow through the boundary at  $x = 1$ . Remarkably, we found no need for entropy stabilization in this test.

### 5.2. Euler equations in 1D

Let us now consider the 1D compressible Euler equations, a nonlinear hyperbolic system of conservation laws for the density  $\rho$ , momentum  $\rho v$ , and total energy  $\rho E$  of an ideal gas. The pressure  $p$  is given by the equation of state  $p = (\gamma - 1)(\rho E - \frac{1}{2}\rho|v|^2)$ , where  $\gamma = 1.4$  is the adiabatic constant. An invariant domain  $\mathcal{G}$  of the Euler system consists of all states  $u = (\rho, \rho v, \rho E)^\top$  such that  $\rho > 0$  and  $p(u) > 0$ . The linear positivity constraint for  $\rho$  can be

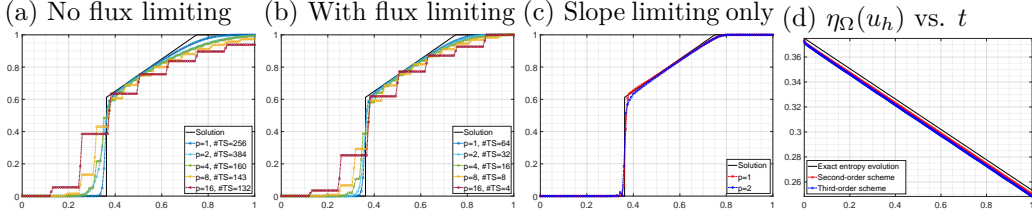


Figure 2: Results for the nonlinear 1D conservation law with the flux function (54) and  $u_0(x) = \chi_{x \geq 1/4}$ . Low-order (a,b) and slope-limited (c) solutions at  $t = 1$ . All approximations use  $N_h = 129$  nodes. The number of employed time steps is denoted by #TS. The entropy evolution history is plotted in panel (d).

enforced as in the scalar case. To ensure positivity preservation for  $p(u)$ , we adapt the limiter proposed by Abgrall et al. [3, 57] to our purposes.

Our numerical tests for the Euler equations are restricted to 1D in this work. We intend to perform 2D tests and extend the proposed methodology to high-order LGL spectral elements in a subsequent publication.

### 5.2.1. Modified Sod's shock tube

In the first test for the Euler equations, we consider a 1D Riemann problem corresponding to a modification [55, Sec. 6.4] of Sod's shock tube problem [54]. The modified version is more challenging because a sonic point occurs within the rarefaction wave region. As a consequence, numerical methods that lack entropy stability tend to produce entropy shocks.

The constant initial states of the modified Sod problem are given by

$$(\rho_0, v_0, p_0)(x) = \begin{cases} (1, 0.75, 1) & \text{if } x < 0.25, \\ (0.125, 0, 0.1) & \text{otherwise.} \end{cases}$$

The left boundary of the domain  $\Omega = (0, 1)$  is a supersonic inlet, at which the values of the primitive variables are determined by the left initial state of the Riemann problem. The boundary data  $\hat{u}$  for  $x = 1$  may be set equal to the right initial state, since the final time  $t = 0.2$  is too short for the waves to reach the right boundary. The exact entropy solution features a rarefaction, a contact, and a shock wave. Its derivation can be found in [55, Ch. 4].

We solve this test problem with the target scheme and its slope-limited counterpart using  $N_h = 129$  degrees of freedom per variable and  $p \in \{1, 2\}$ . The results displayed in Figs. 3a and 3b are in good agreement with the vanishing viscosity solution. Similarly to the test problem considered in



Section 5.1.2, the use of  $\mathbb{P}_1$  elements and fine grids is the best option in this example. While higher-order approximations on coarser grids perform well for rarefaction waves, they are typically more diffusive at discontinuities.

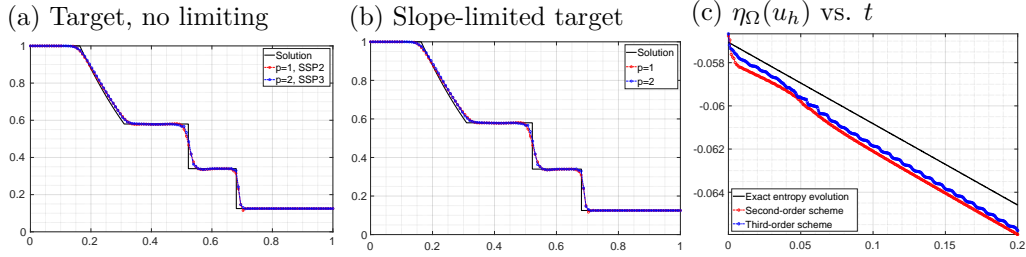


Figure 3: Modified shock tube of Sod, density at  $t = 0.2$  (a,b) and entropy evolution (c) computed with  $N_h = 129$  unknowns per variable.

In Fig. 3c, we plot the evolution of  $\eta_\Omega(u) = \frac{1}{1-\gamma} \int_\Omega \rho s(u) dx$ , where  $s(u) = \log(p\rho^{-\gamma})$  is the specific physical entropy. In contrast to the test case considered in Section 5.1.2, the entropy flux  $q(u) = \rho v s / (1 - \gamma)$  vanishes at the boundaries, as long as the states  $u(0, t)$  and  $u(1, t)$  remain equal to the corresponding initial states of the Riemann problem. On the time interval for which this is the case, the total entropy  $\eta_\Omega(u)$  of the exact vanishing viscosity solution  $u$  is subject to change only due to entropy losses at the shock and/or contact. Numerically, we observe a general trend of entropy dissipation but  $\eta_\Omega(u_h)$  does not decrease monotonically. A probable cause of this behavior is the lack of local entropy stability, which can be cured by adding entropy viscosity or using limiter-based entropy fixes [32]. However, the small wiggles in the evolution of  $\eta_\Omega(u_h)$  are no major concern, since no entropy shocks are observed and  $\eta_\Omega(u_h) \leq \eta_\Omega(u)$ . As demonstrated already in [36] in the context of scalar problems, the WENO stabilization term of our method dissipates enough entropy in most cases. Although additional entropy stabilization may still be appropriate for some scalar problems (such as the challenging but artificial KPP test in Section 5.3.2), we have never observed entropy-violating behavior of IDP finite element schemes for the Euler equations.

### 5.2.2. Woodward–Colella blast wave problem

The 1D blast wave problem [58] is a challenging test for the Euler equations due to strong jumps in the piecewise-constant initial pressure

$$p_0(x) = \begin{cases} 1000 & \text{if } 0 < x < 0.1, \\ 0.01 & \text{if } 0.1 < x < 0.9, \\ 100 & \text{if } 0.9 < x < 1. \end{cases}$$

The initial density is  $\rho_0 \equiv 1$ , and the fluid is at rest, i.e.,  $v_0 \equiv 0$ . The domain  $\Omega = (0, 1)$  has reflecting boundaries at both end points. For short time intervals, the exact solution can be obtained as for any Riemann problem of the Euler equations [55, Ch. 4]. However, by the final time  $t = 0.038$ , interactions with the boundaries and collisions of waves generated by the two Riemann problems result in the unavailability of an exact solution.

We solve this test problem numerically using  $N_h = 1001$  degrees of freedom per variable and  $p \in \{1, 2\}$ . The density profile calculated with the target scheme is shown in Fig. 4a. Since no slope limiting is performed in this experiment, some negative pressures arise during the simulation run. The code does not crash only because we calculate the speed of sound using the formula  $c = \sqrt{\max\{0, \gamma p / \rho\}}$ . This practice is not to be recommended for non-IDP schemes, since it gives rise to consistency errors and disguises unacceptable pressure behavior. Due to round-off errors, a numerical implementation of an IDP scheme might also produce negative pressures of the order of machine precision. In this case, setting  $c := 0$  is an acceptable way to avoid complex-valued solutions. However, such situations did not occur in simulations in which we used the density limiter and the pressure limiter proposed by Abgrall et al. [3]. The slope-limited density profiles shown in Fig. 4b are nonoscillatory, and no negative pressures were generated at any time.

Interestingly enough, the  $\mathbb{P}_2$  version captures the right density peak slightly better than the  $\mathbb{P}_1$  version despite the fact that the initial condition is piecewise constant. This observation further motivates the use of high-order methods for applications in which complex flow patterns are expected to arise.

### 5.2.3. Shu–Osher test / sine-shock interaction

Next, we perform simulations for the popular Shu–Osher test problem [53], which uses the initial condition

$$(\rho_0, v_0, p_0)(x) = \begin{cases} (3.857143, 2.629369, 10.33333) & \text{if } x < -4, \\ (1 + 0.2 \sin(5x), 0, 1) & \text{otherwise} \end{cases}$$

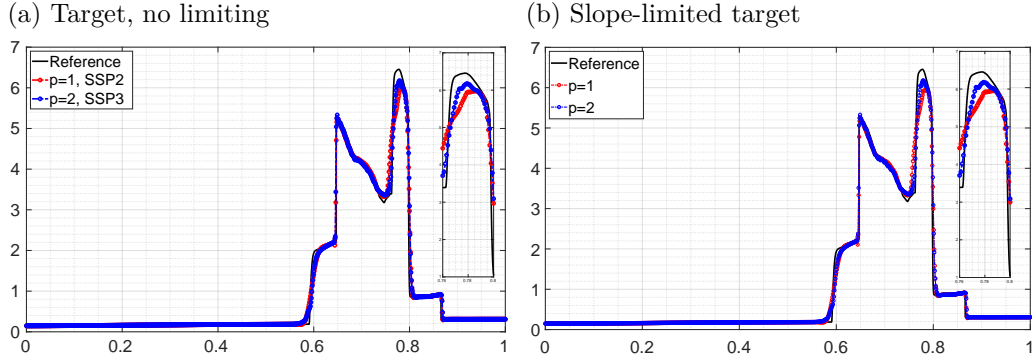


Figure 4: Density profiles for the 1D blast wave problem at  $t = 0.038$  computed with  $N_h = 1001$ .

for the 1D Euler equations to be solved in the domain  $\Omega = (-5, 5)$ . Up to the final time  $t = 1.8$  that is typically used for this test, both boundary conditions can be defined using a Riemann solver with the external state  $\hat{u} = u$ . Reference solutions exhibit a right-propagating shock wave with a post-shock region in which the density is highly oscillatory but smooth.

We test the methods under investigation using  $p \in \{1, 2\}$  and  $N_h = 501$  degrees of freedom per variable. Since the exact solution can be captured well by the target scheme, no violations of IDP constraints occur during the simulation run without the slope limiter. Therefore, the density and pressure fixes are not activated in practice, and the results coincide with those obtained without limiting (see Fig. 5).

It is quite encouraging to see that the  $\mathbb{P}_2$  version captures the post-shock oscillatory region much better than the  $\mathbb{P}_1$  approximation on a mesh with twice as many cells. Furthermore, as is the case for the 1D blast wave problem studied in Section 5.2.2, limiting w. r. t. global bounds does not lead to severe peak clipping effects. However, one can easily think of situations in which this issue is likely to occur, e. g., in simulations of near-vacuum states with quadratic ( $\mathbb{P}_2$ ) or higher order Bernstein elements. As long as the quantities to be limited remain sufficiently far away from the global bounds of IDP constraints, optimal convergence can be achieved with high-order Bernstein elements. In the context of AFC schemes for the advection equation, numerical evidence for the validity of this claim was provided in [17, Sec. 7.1].

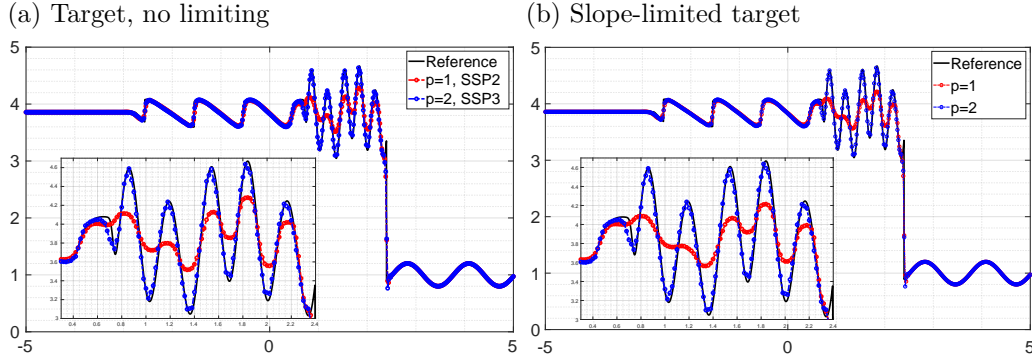


Figure 5: Density profiles for the Shu–Osher test at  $t = 1.8$  computed with  $N_h = 501$ .

### 5.3. Scalar problems in 2D

To evaluate the numerical behavior of the limited CG-WENO scheme and its components in two space dimensions, we consider two additional scalar test problems, one of which is linear and the other one is nonlinear. In both cases, we restrict our studies to  $\mathbb{Q}_1$  finite element approximations, for which the Bernstein and Lagrange basis functions coincide. Computations are performed on uniform meshes with spacing  $h = \frac{1}{128}$ . We use the fake time step  $\Delta t_e = \Delta t_e^{\max}$  defined by (37) and the global time step  $\Delta t = 10^{-3}$ , which satisfies the CFL condition (23) for both test problems. Although our choice of  $\Delta t_e$  exceeds the threshold of Lemma 1, the high-order intermediate cell averages stay in bounds. Therefore, we deactivate the flux limiter for (41) by setting  $\alpha_{ee'} := 1 \ \forall e \in \mathcal{B}_e$ , as proposed in Remark 1.

Since second-order accuracy is the best we can hope to achieve with the  $\mathbb{Q}_1$  version, we replace the element contributions (42) by

$$f_i^e = \gamma_e \left( m_i^e (u_i - u^e) - \Delta t_e \left[ \int_{K_e} \left( \varphi_i - \frac{m_i^e}{|K_e|} \right) \nabla \cdot \mathbf{f}_h d\mathbf{x} - \int_{K_e} \varphi_i (\dot{u}_h^L - \dot{u}_i^L) d\mathbf{x} \right] \right), \quad (55)$$

where  $\dot{u}_h^L$  denotes a low-order approximation to the time derivative  $\dot{u}_h$ . This choice is adopted because it corresponds to the second-order target employed in [25]. A decrease in the value of  $\gamma_e \in [0, 1]$  on the right-hand side of (55) increases the levels of low-order Rusanov dissipation (15), while decreasing the levels of high-order stabilization via the terms depending on  $\Delta t_e$ .

In our presentation of numerical results for two-dimensional hyperbolic problems, the methods under investigation are labeled as follows:

- LO: low-order scheme corresponding to  $\gamma_e = \beta_e = 0$ ;
- HO: high-order scheme corresponding to  $\gamma_e = \beta_e = 1$ ;
- WENO: constrains (55) using  $\gamma_e$  defined by (7), sets  $\beta_e = 1$ ;
- WENO-L: constrains (55) using  $\gamma_e$  and  $\beta_e$  defined by (7) and (51),(52) with global bounds, respectively.

In the WENO version, we use the linear weights  $w_l^{e,\text{lin}} = 0.2$  for  $l = 1, \dots, n_e$  and set  $w_0^{e,\text{lin}} = 1 - \sum_{l=1}^{n_e} w_l^{e,\text{lin}}$ . To study the dependence of the results on the parameter  $q \geq 1$  of formula (7), we run simulations for  $q \in \{3, 5, 10\}$ . The range of approximate solutions is reported in the figures to quantify the levels of numerical diffusion and the magnitude of undershoots/overshoots.

#### 5.3.1. Solid body rotation

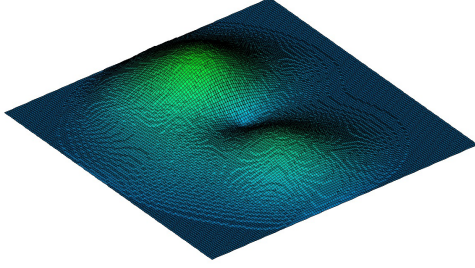
The solid body rotation problem introduced by LeVeque [37] is widely used to assess the ability of numerical methods to capture smooth and discontinuous shapes of an exact solution to the linear advection equation

$$\frac{\partial u}{\partial t} + \nabla \cdot (\mathbf{v}u) = 0 \quad \text{in } \Omega = (0, 1)^2$$

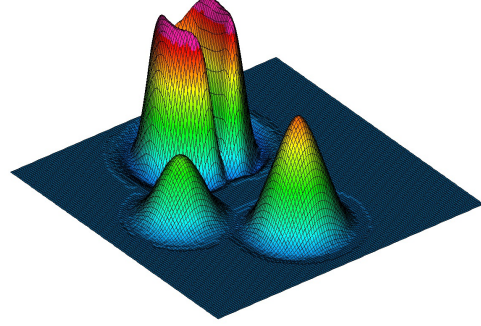
with the velocity field  $\mathbf{v}(x, y) = (0.5 - y, x - 0.5)^\top$ . The initial and boundary conditions for this test are defined in [25, 37]. We stop computations at the final time  $t = 2\pi$ , at which the exact solution coincides with the initial data. The invariant domain to be preserved is the interval  $\mathcal{G} = [0, 1]$ .

The numerical results presented in Fig. 6 show that the low-order (LO) scheme is IDP but too diffusive, while the high-order (HO) target produces undershoots and overshoots that are clearly visible even in the eyeball norm. The WENO results are remarkably accurate and almost IDP for  $q = 3$ . However, violations of the global bounds  $u^{\min} = 0$  and  $u^{\max} = 1$  become more pronounced as the value of  $q$  is increased to 5 and 10. The WENO-L solution is both nonoscillatory and IDP. Hence, our slope limiting strategy eliminates the risk of failure due to ‘greedy’ choices of WENO parameters.

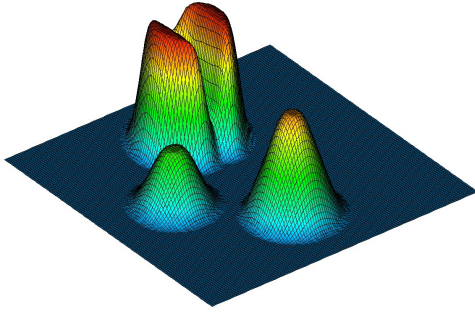
(a) LO,  $u_h \in [0.0, 0.39]$



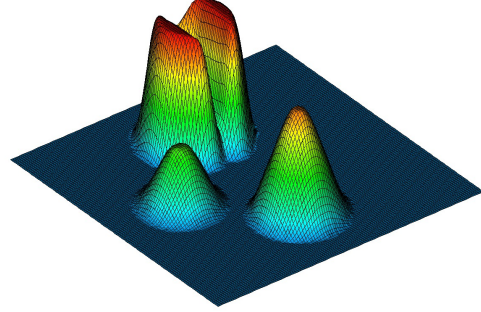
(b) HO,  $u_h \in [-0.06, 1.12]$



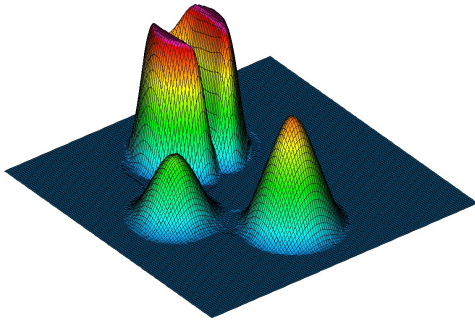
(c) WENO,  $q = 3$ ,  
 $u_h \in [-6.26\text{e-}10, 0.96672]$



(d) WENO,  $q = 5$ ,  
 $u_h \in [-8.80\text{e-}5, 0.99615]$



(e) WENO,  $q = 10$ ,  
 $u_h \in [-7.03\text{e-}3, 1.03601]$



(f) WENO-L,  $q = 10$ ,  
 $u_h \in [0.0, 0.99989]$

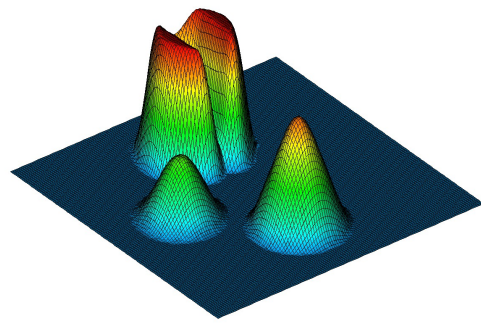


Figure 6: Numerical solutions to the solid body rotation problem [37] at  $t = 2\pi$  calculated using a uniform mesh,  $\mathbb{Q}_1$  elements,  $h = \frac{1}{128}$  and  $\Delta t = 10^{-3}$ .

### 5.3.2. KPP problem

Extending our experiments to nonlinear scalar equations of the form (1a) in 2D, we consider the KPP problem [23], in which  $\mathbf{f}(u) = (\sin(u), \cos(u))$  and  $\Omega = (-2, 2) \times (-2.5, 1.5)$ . The initial condition is given by

$$u_0(x, y) = \begin{cases} \frac{7\pi}{2} & \text{if } \sqrt{x^2 + y^2} \leq 1, \\ \frac{\pi}{4} & \text{otherwise.} \end{cases}$$

At the final time  $t = 1$  the exact entropy solution of the KPP problem exhibits a spiral-shaped shock structure, which is captured correctly by WENO schemes only for the conservative choice  $q = 1$  of the steepening parameter (not shown here). To avoid convergence to spurious weak solutions for larger values of  $q$ , we replace the sensor  $\gamma_e$  of formula (55) by  $\min\{\gamma_e, \xi_e\}$ , where  $\xi_e$  is an entropy correction factor. Using the nodal sensors  $R_i$  of entropy viscosity stabilization employed in [9] and [34, Eq. 51], we set  $\xi_e = \min_{i \in \mathcal{N}_e} R_i$ .

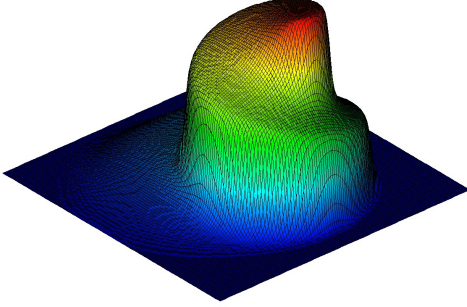
Figure 7 shows the entropy-satisfying low-order solution, the entropy-violating high-order solution, and the WENO results for the KPP problem. Similarly to the linear solid body rotation test, the global maximum and minimum of the initial data are preserved for  $q = 3$ . The solutions obtained with  $q = 5$  and  $q = 10$  without limiting exhibit undershoots and overshoots. The use of slope limiting in the WENO-L version ensures the IDP property without having any negative impact on the accuracy of the results.

## 6. Conclusions

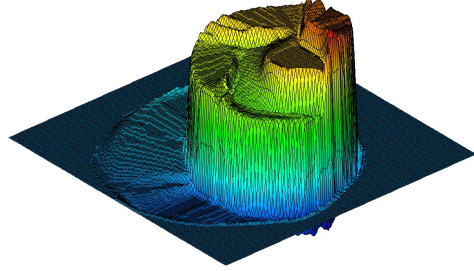
In this paper, we have shown that continuous Galerkin methods can be limited in much the same way as their DG counterparts. Our definition of the intermediate cell averages leads to a fully multidimensional generalization of the bar states that represent averaged exact solutions of projected Riemann problems. The new convex limiting framework enables us to ensure preservation of invariant domains and high-order accuracy without using matrix-based graph viscosity and decomposing antidiffusive element contributions into subcell fluxes. Spurious oscillations are avoided by using dissipative WENO stabilization instead of subcell flux limiters with local bounds. The coarse-cell CFL condition for the flux-limited version of our CG scheme is independent of the basis and weaker than the subcell CFL condition that guarantees the IDP property for Bernstein finite elements in the absence of flux limiting. In



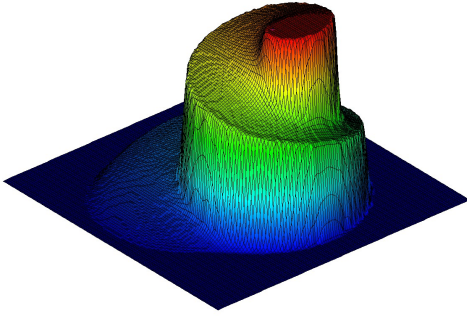
(a) LO,  $u_h \in [0.785, 10.885]$



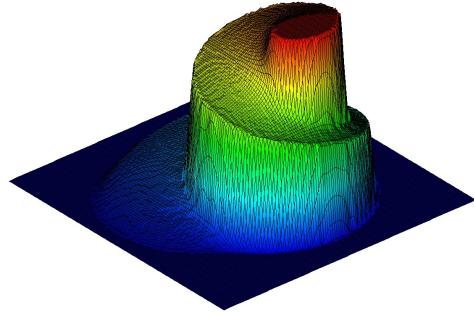
(b) HO,  $u_h \in [-2.054, 14.547]$



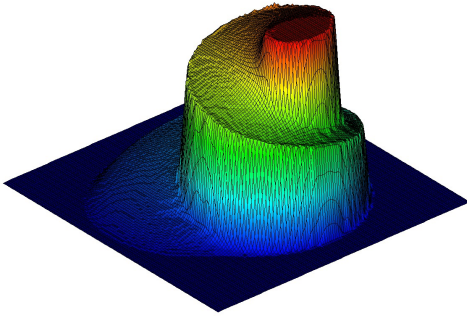
(c) WENO,  $q = 3$ ,  
 $u_h \in [0.785, 10.997]$



(d) WENO,  $q = 5$ ,  
 $u_h \in [0.781, 11.006]$



(e) WENO,  $q = 10$ ,  
 $u_h \in [0.759, 11.050]$



(f) WENO-L,  $q = 10$ ,  
 $u_h \in [0.785, 10.996]$

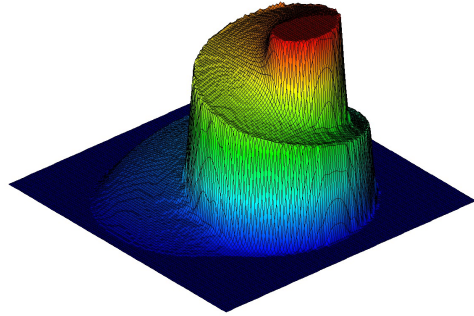


Figure 7: Numerical solutions to the KPP problem [23] at  $t = 1$  calculated using a uniform mesh,  $\mathbb{Q}_1$  elements,  $h = \frac{1}{128}$  and  $\Delta t = 10^{-3}$ .



slope-limited high-order extensions, the CFL condition that ensures nonlinear stability of the underlying target scheme should be taken into account.

Even more significant efficiency gains can presumably be achieved for CG-LGL finite element schemes, because the nonuniform distribution of nodes within the cell makes the subcell CFL condition far more restrictive than that for the uniform submesh of Bernstein nodes [15]. Furthermore, the imposition of global bounds on LGL nodal states is less restrictive than the corresponding inequality constraints for Bernstein nodes. Hence, it is less likely that convex limiting will degrade the rates of convergence to smooth solutions. Adaptation of the proposed algorithms to the LGL setting is straightforward. Regardless of the basis, the performance of practical implementations can be greatly improved by exploiting the matrix-free nature of the presented methods and the data locality of high-order finite element approximations [4, 6, 22].

## Acknowledgments

The work of Dmitri Kuzmin was supported by the German Research Foundation (DFG) within the framework of the priority research program SPP 2410 under grant KU 1530/30-1. Hennes Hajduk participated in this project in his capacity as an associate member of SPP 2410.

## References

- [1] R. Abgrall. Essentially non-oscillatory residual distribution schemes for hyperbolic problems. *J. Comput. Phys.*, 214:773–808, 2006.
- [2] R. Abgrall. High order schemes for hyperbolic problems using globally continuous approximation and avoiding mass matrices. *J. Sci. Comput.*, 73:461–494, 2017.
- [3] R. Abgrall, M. Jiao, Y. Liu, and K. Wu. Bound preserving Point-Average-Moment Polynomial-interpreted (PAMPA) scheme: One-dimensional case. *Preprint arXiv:2410.14292*, 2024.
- [4] J. Andrej, N. Atallah, J.-P. Bäcker, J.-S. Camier, D. Copeland, V. Dobrev, Y. Dudouit, T. Duswald, B. Keith, D. Kim, T. Kolev, B. Lazarov, K. Mittal, W. Pazner, S. Petrides, S. Shiraiwa, M. Stowell, and V. Tomov. High-performance finite elements with MFEM. *Int. J. High Perform. Comput. Appl.*, 38:447–467, 2024.

- [5] T. J. Barth and D. C. Jespersen. The design and application of upwind schemes on unstructured meshes. In *27th Aerospace Sciences Meeting*. American Institute of Aeronautics and Astronautics, 1989.
- [6] P. D. Bello-Maldonado, T. V. Kolev, R. N. Rieben, and V. Z. Tomov. A matrix-free hyperviscosity formulation for high-order ALE hydrodynamics. *Comput. Fluids*, 205:104577, 2020.
- [7] C. J. Cotter and D. Kuzmin. Embedded discontinuous Galerkin transport schemes with localised limiters. *J. Comput. Phys.*, 311:363–373, 2016.
- [8] V. Dobrev, T. Kolev, D. Kuzmin, R. Rieben, and V. Tomov. Sequential limiting in continuous and discontinuous Galerkin methods for the Euler equations. *J. Comput. Phys.*, 356:372–390, 2018.
- [9] J.-L. Guermond, M. Nazarov, B. Popov, and I. Tomas. Second-order invariant domain preserving approximation of the Euler equations using convex limiting. *SIAM J. Sci. Comput.*, 40:A3211–A3239, 2018.
- [10] J.-L. Guermond, R. Pasquetti, and B. Popov. Entropy viscosity method for nonlinear conservation laws. *J. Comput. Phys.*, 230:4248–4267, 2011.
- [11] J.-L. Guermond and B. Popov. Invariant domains and first-order continuous finite element approximation for hyperbolic systems. *SIAM J. Numer. Anal.*, 54:2466–2489, 2016.
- [12] J.-L. Guermond and B. Popov. Invariant domains and second-order continuous finite element approximation for scalar conservation equations. *SIAM J. Numer. Anal.*, 55:3120–3146, 2017.
- [13] J.-L. Guermond, B. Popov, and I. Tomas. Invariant domain preserving discretization-independent schemes and convex limiting for hyperbolic systems. *Comput. Methods Appl. Mech. Eng.*, 347:143–175, 2019.
- [14] H. Hajduk. Monolithic convex limiting in discontinuous Galerkin discretizations of hyperbolic conservation laws. *Comput. Math. Appl.*, 87:120–138, 2021.
- [15] H. Hajduk. Improvements of algebraic flux-correction schemes based on Bernstein finite elements. *J. Numer. Math.*, 2025.

- [16] H. Hajduk, D. Kuzmin, T. Kolev, and R. Abgrall. Matrix-free subcell residual distribution for Bernstein finite element discretizations of linear advection equations. *Comput. Methods Appl. Mech. Eng.*, 359:112658, 2020.
- [17] H. Hajduk, D. Kuzmin, T. Kolev, V. Tomov, I. Tomas, and J. N. Shadid. Matrix-free subcell residual distribution for Bernstein finite elements: Monolithic limiting. *Comput. Fluids*, 200:104451, 2020.
- [18] D. Hoff. A finite difference scheme for a system of two conservation laws with artificial viscosity. *Math. Comput.*, 33:1171–1193, 1979.
- [19] T. Hughes, G. Scovazzi, and T. Tezduyar. Stabilized methods for compressible flows. *J. Sci. Comput.*, 43(3):343–368, 2010.
- [20] G.-S. Jiang and C.-W. Shu. Efficient implementation of weighted ENO schemes. *J. Comput. Phys.*, 126:202–228, 1996.
- [21] C. Johnson, A. Szepessy, and P. Hansbo. On the convergence of shock-capturing streamline diffusion finite element methods for hyperbolic conservation laws. *Math. Comput.*, 54:107–129, 1990.
- [22] M. Kronbichler and K. Kormann. Fast matrix-free evaluation of discontinuous Galerkin finite element operators. *ACM Trans. Math. Softw.*, 45:1–40, 2019.
- [23] A. Kurganov, G. Petrova, and B. Popov. Adaptive semidiscrete central-upwind schemes for nonconvex hyperbolic conservation laws. *SIAM J. Sci. Comput.*, 29:2381–2401, 2007.
- [24] D. Kuzmin. A vertex-based hierarchical slope limiter for p-adaptive discontinuous Galerkin methods. *J. Comput. Appl. Math.*, 233:3077–3085, 2010.
- [25] D. Kuzmin. Monolithic convex limiting for continuous finite element discretizations of hyperbolic conservation laws. *Comput. Methods Appl. Mech. Eng.*, 361:112804, 2020.
- [26] D. Kuzmin. A new perspective on flux and slope limiting in discontinuous Galerkin methods for hyperbolic conservation laws. *Comput. Methods Appl. Mech. Eng.*, 373:113569, 2021.

- [27] D. Kuzmin and H. Hajduk. *Property-Preserving Numerical Schemes for Conservation Laws*. World Scientific, 2023.
- [28] D. Kuzmin, H. Hajduk, and A. Rupp. Locally bound-preserving enriched Galerkin methods for the linear advection equation. *Comput. Fluids*, 205:104525, 2020.
- [29] D. Kuzmin, S. Lee, and Y.-Y. Yang. Bound-preserving and entropy stable enriched Galerkin methods for nonlinear hyperbolic equations. *Preprint arXiv:2411.19160*, 2024.
- [30] D. Kuzmin, M. Möller, and M. Garris. Algebraic flux correction II. Compressible flow problems. In D. Kuzmin, R. Löhner, and S. Turek, editors, *Flux-Corrected Transport: Principles, Algorithms, and Applications*, pages 193–238. Springer, 2 edition, 2012.
- [31] D. Kuzmin, M. Möller, J. N. Shadid, and M. Shashkov. Failsafe flux limiting and constrained data projections for equations of gas dynamics. *J. Comput. Phys.*, 229:8766–8779, 2010.
- [32] D. Kuzmin and M. Quezada de Luna. Algebraic entropy fixes and convex limiting for continuous finite element discretizations of scalar hyperbolic conservation laws. *Comput. Methods Appl. Mech. Eng.*, 372:113370, 2020.
- [33] D. Kuzmin and M. Quezada de Luna. Entropy conservation property and entropy stabilization of high-order continuous Galerkin approximations to scalar conservation laws. *Comput. Fluids*, 213:104742, 2020.
- [34] D. Kuzmin and M. Quezada de Luna. Subcell flux limiting for high-order Bernstein finite element discretizations of scalar hyperbolic conservation laws. *J. Comput. Phys.*, 411:109411, 2020.
- [35] D. Kuzmin, M. Quezada de Luna, D. I. Ketcheson, and J. Gröll. Bound-preserving flux limiting for high-order explicit Runge–Kutta time discretizations of hyperbolic conservation laws. *J. Sci. Comput.*, 91, 2022.
- [36] D. Kuzmin and J. Vedral. Dissipation-based WENO stabilization of high-order finite element methods for scalar conservation laws. *J. Comput. Phys.*, 487:112153, 2023.

- [37] R. J. LeVeque. High-resolution conservative algorithms for advection in incompressible flow. *SIAM J. Numer. Anal.*, 33:627–665, 1996.
- [38] Y. Lin and J. Chan. High order entropy stable discontinuous Galerkin spectral element methods through subcell limiting. *J. Comput. Phys.*, 498:112677, 2024.
- [39] C. Lohmann and D. Kuzmin. Synchronized flux limiting for gas dynamics variables. *J. Comput. Phys.*, 326:973–990, 2016.
- [40] C. Lohmann, D. Kuzmin, J. N. Shadid, and S. Mabuza. Flux-corrected transport algorithms for continuous Galerkin methods based on high order Bernstein finite elements. *J. Comput. Phys.*, 344:151–186, 2017.
- [41] R. Löhner, K. Morgan, J. Peraire, and M. Vahdati. Finite element flux-corrected transport (FEM-FCT) for the Euler and Navier–Stokes equations. *Int. J. Numer. Meth. Fluids*, 7:1093–1109, 1987.
- [42] H. Luo, J. D. Baum, and R. Löhner. Edge-based finite element scheme for the Euler equations. *AIAA J.*, 32:1183–1190, 1994.
- [43] H. Luo, J. D. Baum, and R. Löhner. A Hermite WENO-based limiter for discontinuous Galerkin method on unstructured grids. *J. Comput. Phys.*, 225:686–713, 2007.
- [44] S. A. Moe, J. A. Rossmanith, and D. C. Seal. Positivity-preserving discontinuous Galerkin methods with Lax–Wendroff time discretizations. *J. Sci. Comput.*, 71:44–70, 2017.
- [45] P. Moujaes and D. Kuzmin. Monolithic convex limiting and implicit pseudo-time stepping for calculating steady-state solutions of the Euler equations. *J. Comput. Phys.*, 523:113687, 2025.
- [46] M. Olshanskii, J.-P. Bäcker, and D. Kuzmin. Gradient-penalty stabilization of sharp and diffuse interface formulations in unfitted Nitsche finite element methods. *Preprint arXiv:2501.16594*, 2025.
- [47] W. Pazner. Sparse invariant domain preserving discontinuous Galerkin methods with subcell convex limiting. *Comput. Methods Appl. Mech. Eng.*, 382:113876, 2021.

- [48] B. Perthame and C.-W. Shu. On positivity preserving finite volume schemes for Euler equations. *Numer. Math.*, 73:119–130, 1996.
- [49] J. Qiu and C.-W. Shu. Runge–Kutta discontinuous Galerkin method using WENO limiters. *SIAM J. Sci. Comput.*, 26:907–929, 2005.
- [50] M. Quezada de Luna and D. I. Ketcheson. Maximum principle preserving space and time flux limiting for diagonally implicit Runge–Kutta discretizations of scalar convection-diffusion equations. *J. Sci. Comput.*, 92:102, 2022.
- [51] A. M. Rueda-Ramírez, B. Bolm, D. Kuzmin, and G. J. Gassner. Monolithic convex limiting for Legendre–Gauss–Lobatto discontinuous Galerkin spectral-element methods. *Commun. Appl. Math. Comput.*, 6:1860–1898, 2024.
- [52] C.-W. Shu. High order WENO and DG methods for time-dependent convection-dominated PDEs: A brief survey of several recent developments. *J. Comput. Phys.*, 316:598–613, 2016.
- [53] C.-W. Shu and S. Osher. Efficient implementation of essentially non-oscillatory shock-capturing schemes, II. In *Upwind and High-Resolution Schemes*, pages 328–374. Springer, 1989.
- [54] G. A. Sod. A survey of several finite difference methods for systems of nonlinear hyperbolic conservation laws. *J. Comput. Phys.*, 27:1–31, 1978.
- [55] E. F. Toro. *Riemann Solvers and Numerical Methods for Fluid Dynamics*. Springer, 3 edition, 2009.
- [56] J. Vedral, A. Rupp, and D. Kuzmin. Strongly consistent low-dissipation WENO schemes for finite elements. *Appl. Numer. Math.*, 210:64–81, 2025.
- [57] G. Wissocq, Y. Liu, and R. Abgrall. A positive-and bound-preserving vectorial lattice Boltzmann method in two dimensions. *Preprint arXiv:2411.15001*, 2024.
- [58] P. Woodward and P. Colella. The numerical simulation of two-dimensional fluid flow with strong shocks. *J. Comput. Phys.*, 54:115–173, 1984.

- [59] K. Wu and C.-W. Shu. Geometric quasilinearization framework for analysis and design of bound-preserving schemes. *SIAM Rev.*, 65:1031–1073, 2023.
- [60] T. Xiong, J.-M. Qiu, and Z. Xu. Parametrized positivity preserving flux limiters for the high order finite difference WENO scheme solving compressible Euler equations. *J. Sci. Comput.*, 67(3):1066–1088, 2016.
- [61] Z. Xu. Parametrized maximum principle preserving flux limiters for high order schemes solving hyperbolic conservation laws: One-dimensional scalar problem. *Math. Comput.*, 83:2213–2238, 2014.
- [62] S. T. Zalesak. Fully multidimensional flux-corrected transport algorithms for fluids. *J. Comput. Phys.*, 31:335–362, 1979.
- [63] X. Zhang and C.-W. Shu. On positivity-preserving high order discontinuous Galerkin schemes for compressible Euler equations on rectangular meshes. *J. Comput. Phys.*, 229:8918–8934, 2010.
- [64] X. Zhang and C.-W. Shu. Maximum-principle-satisfying and positivity-preserving high-order schemes for conservation laws: Survey and new developments. *Proc. R. Soc. A*, 467:2752–2776, 2011.
- [65] X. Zhang, Y. Xia, and C.-W. Shu. Maximum-principle-satisfying and positivity-preserving high order discontinuous Galerkin schemes for conservation laws on triangular meshes. *J. Sci. Comput.*, 50:29–62, 2012.
- [66] X. Zhong and C.-W. Shu. A simple weighted essentially nonoscillatory limiter for Runge–Kutta discontinuous Galerkin methods. *J. Comput. Phys.*, 232:397–415, 2013.
- [67] J. Zhu and J. Qiu. Hermite WENO schemes and their application as limiters for Runge–Kutta discontinuous Galerkin method, III: Unstructured meshes. *J. Sci. Comput.*, 39:293–321, 2009.
- [68] J. Zhu, J. Qiu, C.-W. Shu, and M. Dumbser. Runge–Kutta discontinuous Galerkin method using WENO limiters II: Unstructured meshes. *J. Comput. Phys.*, 227(9):4330–4353, 2008.
- [69] J. Zhu, X. Zhong, C.-W. Shu, and J. Qiu. Runge–Kutta discontinuous Galerkin method with a simple and compact Hermite WENO limiter on unstructured meshes. *Commun. Comput. Phys.*, 21:623–649, 2017.